

# Epigenetic neural glioblastoma enhances synaptic integration and predicts therapeutic vulnerability

Richard Drexler<sup>1,2,†</sup>, Robin Khatri<sup>3,4,†</sup>, Thomas Sauvigny<sup>1</sup>, Malte Mohme<sup>1</sup>, Cecile L. Maire<sup>1</sup>, Alice Ryba<sup>1</sup>, Yahya Zghaibeh<sup>1</sup>, Lasse Dührsen<sup>1</sup>, Amanda Salviano-Silva<sup>1</sup>, Katrin Lamszus<sup>1</sup>, Manfred Westphal<sup>1</sup>, Jens Gempt<sup>1</sup>, Annika K. Wefers<sup>5,6</sup>, Julia Neumann<sup>5,7,8</sup>, Helena Bode<sup>8</sup>, Fabian Hausmann<sup>3,4</sup>, Tobias B. Huber<sup>9,10</sup>, Stefan Bonn<sup>3,4</sup>, Kerstin Jütten<sup>11</sup>, Daniel Delev<sup>11</sup>, Katharina J. Weber<sup>12,13,14,15</sup>, Patrick N. Harter<sup>12,16</sup>, Julia Onken<sup>17</sup>, Peter Vajkoczy<sup>17</sup>, David Capper<sup>18</sup>, Benedikt Wiestler<sup>19</sup>, Michael Weller<sup>20</sup>, Berend Snijder<sup>21</sup>, Alicia Buck<sup>20</sup>, Tobias Weiss<sup>20</sup>, Michael B. Keough<sup>2</sup>, Lijun Ni<sup>2</sup>, Michelle Monje<sup>2</sup>, Dana Silverbush<sup>22</sup>, Volker Hovestadt<sup>22</sup>, Mario L. Suvà<sup>22,23</sup>, Saritha Krishna<sup>24</sup>, Shawn L. Hervey-Jumper<sup>24</sup>, Ulrich Schüller<sup>5,7,8</sup>, Dieter H. Heiland<sup>25,\*</sup>, Sonja Hänzelmann<sup>3,4,9,10,\*</sup>, Franz L. Ricklefs<sup>1,\*</sup>

<sup>1</sup> Department of Neurosurgery, University Medical Center Hamburg-Eppendorf, Hamburg, Germany.

<sup>2</sup> Department of Neurology, Stanford University, Stanford, CA, 94305, USA.

<sup>3</sup> Institute of Medical Systems Biology, University Medical Center Hamburg-Eppendorf, Hamburg, Germany.

<sup>4</sup> Center for Biomedical AI, University Medical Center Hamburg-Eppendorf, Hamburg, Germany.

<sup>5</sup> Institute of Neuropathology, University Medical Center Hamburg-Eppendorf, Hamburg, Germany.

<sup>6</sup> Mildred Scheel Cancer Career Center HaTriCS4, University Medical Center Hamburg-Eppendorf, Hamburg, Germany.

<sup>7</sup> Department of Pediatric Hematology and Oncology, Research Institute Children's Cancer Center Hamburg, University Medical Center Hamburg-Eppendorf, Hamburg, Germany.

<sup>8</sup> Research Institute Children's Cancer Center Hamburg, Hamburg, Germany.

<sup>9</sup> III. Department of Medicine, University Medical Center Hamburg-Eppendorf, Hamburg, Germany.

<sup>10</sup> Hamburg Center for Translational Immunology, University Medical Center Hamburg-Eppendorf, Hamburg, Germany.

<sup>11</sup> Department of Neurosurgery, University Hospital Aachen, Aachen, Germany.

<sup>12</sup> Neurological Institute (Edinger Institute), University Hospital Frankfurt, Frankfurt am Main, Germany.

<sup>13</sup> German Cancer Consortium (DKTK), Heidelberg, Germany and German Cancer Research Center (DKFZ), Heidelberg, Germany

<sup>14</sup> Frankfurt Cancer Institute (FCI), Frankfurt am Main, Germany.

<sup>15</sup> University Cancer Center (UCT) Frankfurt, Frankfurt am Main, Germany.

<sup>16</sup> Institute of Neuropathology, Faculty of Medicine, LMU Munich, Munich, Germany.

<sup>17</sup> Department of Neurosurgery, Charité - Universitätsmedizin Berlin, Berlin, Germany.

<sup>18</sup> Department of Neuropathology, Charité - Universitätsmedizin Berlin, Corporate Member of Freie Universität Berlin and Humboldt-Universität zu Berlin, Charitéplatz 1, 10117 Berlin, Germany.

<sup>19</sup> Department of Neuroradiology, Klinikum rechts der Isar, School of Medicine, Technical University Munich, Munich.

<sup>20a</sup> Department of Neurology, Clinical Neuroscience Center, University Hospital Zurich, Switzerland.

<sup>20b</sup> Department of Neurology, University of Zürich, Switzerland.

<sup>21</sup> Institute of Molecular Systems Biology, ETH Zurich, Zurich, Switzerland

<sup>22</sup> Broad Institute of Harvard and MIT, Cambridge, MA, USA.

<sup>23</sup> Department of Pathology and Center for Cancer Research, Massachusetts General Hospital and Harvard Medical School, Boston, MA, 02114, USA.

<sup>24</sup> Department of Neurological Surgery, University of California, San Francisco, San Francisco, CA, 94143, USA.

<sup>25</sup> Department of Neurosurgery, Medical Center University of Freiburg, Freiburg, Germany.

<sup>†</sup> These authors contributed equally.

<sup>\*</sup> These authors jointly supervised this work.

## Corresponding author:

Franz L. Ricklefs, Department of Neurosurgery, University Medical Center Hamburg-Eppendorf, Martinistrasse 52, 20246 Hamburg, Germany, f.ricklefs@uke.de, phone +49-40-7410-0, fax: +49-40-7410-0

## Keywords:

Glioma, GBM, DMG, DIPG, neuron, cancer neuroscience, connectivity, BDNF, stem cell, neuronal activity, synapse, NPC, OPC

51 **ABSTRACT**

52 Neural-tumor interactions drive glioma growth as evidenced in preclinical models, but clinical  
53 validation is nascent. We present an epigenetically defined neural signature of glioblastoma  
54 that independently affects patients' survival. We use reference signatures of neural cells to  
55 deconvolve tumor DNA and classify samples into low- or high-neural tumors. High-neural  
56 glioblastomas exhibit hypomethylated CpG sites and upregulation of genes associated with  
57 synaptic integration. Single-cell transcriptomic analysis reveals high abundance of stem cell-  
58 like malignant cells classified as oligodendrocyte precursor and neural precursor cell-like in  
59 high-neural glioblastoma. High-neural glioblastoma cells engender neuron-to-glioma synapse  
60 formation *in vitro* and *in vivo* and show an unfavorable survival after xenografting. In patients,  
61 a high-neural signature associates with decreased survival as well as increased functional  
62 connectivity and can be detected via DNA analytes and brain-derived neurotrophic factor in  
63 plasma. Our study presents an epigenetically defined malignant neural signature in high-grade  
64 gliomas that is prognostically relevant.

65

## 66 INTRODUCTION

67 The importance of the nervous system as a key regulator of primary brain and metastatic  
68 tumors has been repeatedly highlighted but has not yet been translated into a therapeutically  
69 relevant setting<sup>1</sup>. The presence of neural-cancer interactions is a contributing factor in  
70 tumorigenesis and progression<sup>1-3</sup>. Particularly in gliomas, studies have demonstrated that the  
71 formation of malignant neuron-to-glioma networks is critical for cancer progression, and have  
72 identified crucial mechanisms such as paracrine signaling via neuroligin-3 (*NLGN-3*) or brain-  
73 derived neurotrophic factor (*BDNF*) and glutamatergic synapses driven by neuronal activity<sup>3-  
74 6</sup>. Additionally, glioma cells remodel neuronal circuits and are able to increase neuronal  
75 hyperexcitability<sup>3,7-10</sup>. Therefore, targeting bidirectional neural-to-cancer interactions may be  
76 a promising therapeutic approach in poor prognosis gliomas, such as isocitrate  
77 dehydrogenase (IDH)-wildtype glioblastoma and H3 K27-altered diffuse midline glioma  
78 (DMG)<sup>11,12</sup>.

79 Despite the increasing appreciation of the importance of neuroscience in understanding brain  
80 tumors, the targetable disruption of neuron-to-cancer synaptic communication in glioma was  
81 initially limited to preclinical models. Further insight into molecular mechanisms of neuron-to-  
82 glioma interactions identified connected and unconnected glioblastoma cells that form two  
83 distinct cell states and differ in their gene signatures as well as functions within neuron-to-  
84 glioma networks<sup>13</sup>. In addition, upregulation of neural signaling programs that promote brain  
85 tumor invasiveness at the time of recurrence has been demonstrated<sup>14</sup>. Recently,  
86 glioblastomas exhibiting high functional connectivity have been shown to be associated with  
87 poorer survival, and thrombospondin-1 (*TSP-1*)-expressing glioma cells have been identified  
88 as a key cell population for promoting neuron-to-glioma interaction<sup>10</sup>. Moreover, callosal  
89 projection neurons were shown to promote glioma progression and widespread infiltration  
90 underpinning the high importance of the central nervous system as a critical regulator and  
91 potential therapeutic target<sup>15</sup>.

92

93 High-grade gliomas are diffuse infiltrating tumors with a cellular composition consisting of both  
94 malignant and non-malignant cells which could be addressed by epigenetic bulk DNA analysis  
95 since it provides the possibility to decipher the underlying cellular composition. We hence  
96 hypothesized that by using brain tumor-related epigenetic signatures, we might decipher the  
97 epigenetic signature of IDH-wildtype high-grade gliomas and proposed that certain epigenetic  
98 subclasses may be more likely to be integrated into neuron-to-glioma networks and that their  
99 stratification may be clinically relevant. To address these hypotheses, we determined the  
100 tumoral neural signature by using a neural reference to screen bulk CNS tumors and stratified  
101 glioblastoma samples into low- and high-neural subgroups. These two distinct neural  
102 subgroups of glioblastoma were further molecularly, functionally, and clinically characterized  
103 by DNA methylation, spatial transcriptomics, single-cell deconvolution, proteomics, and  
104 imaging-based functional connectivity in human as well as *in vitro* and *in vivo* experiments.  
105 We demonstrate that high-neural glioblastomas exhibit a synaptogenic profile and have an  
106 oligodendrocyte-precursor cell (OPC) and neuronal progenitor cell (NPC)-like character with  
107 a malignant stem cell-like state. High-neural glioblastomas show increased functional  
108 connectivity and neuron-to-glioma synapse formation *in vivo* and *in vitro*. Stratification of  
109 patients into low- and high-neural tumors proves to be an independent prognostic factor for  
110 survival in glioblastoma as well as DMG which highlights the clinical relevance of the here  
111 presented epigenetic neural signature.

112

113

114

## 115 RESULTS

116 To address the aforementioned hypotheses, we applied the epigenetic neural signature of  
117 Moss et al<sup>16</sup> to estimate cellular composition (Fig. 1a) of a combined dataset of epigenetically  
118 profiled central nervous system (CNS) tumors of Capper et al.<sup>17</sup> and our institutional cohort  
119 (“clinical cohort”) (Supplementary Fig. 1). Using this combined dataset, IDH-wildtype  
120 glioblastoma samples (n=1058) were selected and dichotomized for defining a cut-off  
121 separating low- and high-neural tumors (cut-off 0.41, Supplementary Fig. 2). This cut-off was  
122 applied to 363 glioblastoma patients from our clinical cohort who received surgical treatment  
123 followed by standard-of-care combined chemo-radiotherapy. Survival analysis revealed a  
124 significantly shorter overall (OS) ( $p < 0.0001$ , median OS 14.2 versus 21.2 months, Fig. 1b)  
125 and progression-free survival (PFS) ( $p = 0.02$ , median PFS 6.2 versus 10.0 months, Fig. 1c)  
126 for patients with a high-neural glioblastoma (Supplementary Table 1). This finding was  
127 replicated in an external cohort with 187 patients from the TCGA-GBM database<sup>18</sup> who  
128 received adjuvant combined chemo-radiotherapy ( $p < 0.01$ , median OS 12.0 versus 17.1  
129 months, Fig. 1d). Additionally, the neural classification was identified as an independent  
130 prognostic factor for OS (OR; 95% CI: 1.96; 1.45-2.64,  $p < 0.01$ , Fig. 1e) and PFS (OR; 95%  
131 CI: 1.51; 1.13-2.02,  $p < 0.01$ , Fig. 1f) next to established factors such as extent of resection  
132 (EOR), and O6-methylguanine-DNA-methyltransferase (*MGMT*) promoter methylation status  
133 (Supplementary Tables 2 and 3). Other infiltrating brain tumor cell types of the lymphoid or  
134 myeloid lineage did not show an association with patient survival (Supplementary Fig. 3).  
135

136 ***High-neural glioblastoma exhibits a synaptogenic and OPC-/NPC-like character***

137 To further understand the survival difference and to demonstrate validity of the neural  
138 signature as a prognostic marker, we applied the “invasivity signature” by Venkataramani et  
139 al.<sup>13</sup> which describes 172 genes associated with neural features, migration, and invasion  
140 (Extended Data 1) to the DNA methylation data of our clinical cohort. High-neural tumors were  
141 hypomethylated at CpG sites within gene loci of the invasivity signature (Fig. 2a). Additionally,  
142 two gene sets that are either associated with neuron-to-glioma synapse formation<sup>11</sup> (“neuronal  
143 signature genes”, Extended Data 2) or relevant to trans-synaptic signaling<sup>19</sup> (“trans-synaptic  
144 signaling genes”, Extended Data 3) were hypomethylated in high-neural glioblastomas  
145 (Supplementary Fig. 4a). Tumor DNA purity correlated with the neural signature, ruling out the  
146 possibility of sample contamination by non-malignant neural cells ( $p < 0.01$ ,  $R^2 = 0.38$   
147 Supplementary Fig. 4b).

148

149 Next, we used an integrative analysis of both epigenetic and transcriptomic datasets of  
150 glioblastoma samples (TCGA). Applying weighted correlation network analysis (WGCNA), we  
151 identified three expression modules significantly correlated with the epigenetic status of high-  
152 neural glioblastoma (Fig. 2a). Module green ( $R^2=0.55$   $p=3.5 \times 10^{-6}$ ), Module cyan ( $R^2=0.67$   
153  $p<2.2 \times 10^{-22}$ ) and Module midnightblue ( $R^2=0.41$   $p=9.3 \times 10^{-5}$ ) (Fig. 2b-c). Gene ontology  
154 analysis revealed that these modules were associated with synaptic functions (*GRIN3A*,  
155 *SYT4*, *SNAP25*), regulating the expression of genes involved in neuronal differentiation  
156 (*NEUROD2*) and calcium-dependent cell adhesion (*CDH22*, *CNTNAP5* and *CNTN3*) (Fig. 2d-  
157 f). When projecting the module eigengene signatures onto a single cell dataset, malignant  
158 neural precursor cells (NPC)-like and oligodendrocyte precursor cell (OPC)-like (module green  
159 and cyan  $p<0.01$ ) as well as non-malignant oligodendrocytes (module midnightblue  $p<0.01$ ),  
160 revealed significant enrichment of the corresponding expression modules (Fig. 2g-i).

161

162 This pro-synaptogenesis signature of high-neural glioblastoma based on epigenetic and  
163 transcriptomic data was further validated in the tumor proteome by mass spectrometry  
164 analysis of 28 glioblastoma samples (low-neural: n = 18, high-neural: n = 10) (Supplementary  
165 Fig. 4c-h). High-neural glioblastoma exhibited increased proteins connected to synaptic  
166 transmission and vesicle-mediated transsynaptic signaling (Supplementary Fig. 4f). As  
167 previously seen in the spatial transcriptomic analysis, an OPC- and NPC-like character was  
168 evident in the high-neural glioblastoma cells after transfer to a single-cell data set  
169 (Supplementary Fig. 4g), as well as a malignant signature within these cells (Supplementary  
170 Fig. 4h).

171

172 To further investigate the spatial organization, we employed spatially resolved  
173 transcriptomics<sup>20</sup> to samples which were epigenetically characterized as low- or high-neural  
174 glioblastoma (Fig. 3a-d). We observed a distinct spatial enrichment of the eigengene  
175 signatures from the green and cyan modules along with significant spatial correlation with the  
176 spatial OPC and neuronal development niches in high-neural tumors. Conversely, we  
177 confirmed the increased enrichment of low-neural glioblastoma expression modules in close  
178 relation to the necrotic core (Fig. 3a-b). These modules also spatially correlate with  
179 inflammation and metabolic alterations (Fig. 3c). To dissect the differences in cellular  
180 hierarchies and proximity between low- and high-neural glioblastoma, we computed cellular  
181 neighborhood graphs derived from single-cell deconvolution<sup>21</sup> from samples which were  
182 epigenetically defined as low- and high-neural glioblastoma. Our observations indicated that  
183 the overall architecture of the tumors maintained similar (Fig. 3a-b), however, a more intricate  
184 interface between NPC/OPC-like cells and the non-malignant neuronal environment was  
185 evident only within high-neural glioblastoma (Fig. 3c-d).

186

187 ***Analysis of the cell composition reveals an enriched stem cell-like state in high-***  
188 ***neural glioblastoma***

189 Brain tumor cells with a high neural state exhibit multiple neural features associated with  
190 neurodevelopmental programs<sup>1</sup>. We used a non-reference-based multi-dimensional single-  
191 cell deconvolution algorithm (see Methods) to further investigate the developmental status of  
192 our low- and high-neural glioblastoma samples. Here, a higher stem/progenitor cell-like  
193 component in the high-neural glioblastoma was observed (28.05%) compared to all newly  
194 diagnosed glioblastoma (17.31%) and low-neural glioblastoma (14.14%) (Fig. 3e). In contrast,  
195 the immune compartment was lower in high-neural glioblastoma (8.84% versus 20.77%  
196 versus 24.05%, Fig. 3e). We further determined a significant correlation of the neural signature  
197 with the stem cell component ( $p < 0.001$ ,  $R^2 = 0.06$ , Fig. 3f) and a significantly lower immune  
198 cell component ( $p < 0.001$ ,  $R^2 = 0.15$ , Fig. 3g). Copy number variations (CNV) of all  
199 glioblastoma samples were computed using the Conumee R package 1.28.0<sup>22</sup>. Tumors with  
200 a high and low-neural signature showed no significant differences in copy number variation  
201 (CNV) (Supplementary Fig. 5), further increasing the relevance of epigenetic signatures.

202

203 ***High-neural glioblastoma engenders increased neuron-to-glioma***  
204 ***synaptogenesis and worse survival in patient-derived xenograft models***

205 Most studies elucidating the biology of cancer neuroscience in high-grade glioma were  
206 performed in preclinical models. We therefore examined the translatability of our neural  
207 classification to cell cultures and patient-derived xenograft (PDX) models. To this end, we  
208 analyzed the neural signature in cell cultures obtained from fresh samples of 17 glioblastoma  
209 patients and observed a well-preserved neural signature in 82.3% of our cell cultures  
210 compared to the original tumor samples (Fig. 4a-b). Analysis of cellular components by single-  
211 cell deconvolution revealed that *in vitro* culturing of tumor cells excluded the immune  
212 component and decreased the glial component, while the neural component remained stable,  
213 further supporting the epigenetically imprinted neural signature of glioblastoma cells (Fig. 4c).



214 In addition, the neural signature remained stable in long-term cultures ( $p > 0.05$ , Fig. 4d).  
215 Comparison of low- and high-neural glioblastoma in PDX mouse models of an internal cohort  
216 ( $n=30$  mice of 7 patient-derived glioblastoma cell cultures, Fig. 4e) and two publicly available  
217 cohorts<sup>23,24</sup> ( $n=96$  patient-derived glioblastoma cell cultures, Fig. 4f) showed a significantly  
218 shorter survival of mice bearing high-neural tumors (internal cohort:  $p = 0.0009$ , external  
219 cohort:  $p = 0.001$ ). These findings are consistent with the recent report of shorter survival in  
220 mice bearing orthotopic high functional connectivity (HFC) xenografts compared to those  
221 bearing low functional connectivity (LFC) xenografts<sup>10</sup>. In our study, an increased tumor  
222 burden assessed by Ki67<sup>+</sup>/HNA<sup>+</sup> proliferation index ( $p < 0.01$ , Fig. 4g-i) and increased co-  
223 localization of neuron-to-glioma synapse puncta ( $p < 0.01$ , Fig. 4j-k) were seen in high-neural  
224 glioblastoma after injection of primary patient-derived cells of both neural subgroups in  
225 immunodeficient mice ( $n=5$  per subgroup). The increased formation of neuron-to-glioma  
226 synapses in high-neural glioblastoma was additionally proven using electron microscopy in  
227 red fluorescent protein (RFP)-labelled, patient-derived low- and high-neural xenografts ( $n = 3$   
228 per group,  $p = 0.008$ , Fig. 4l). In accordance with our *in vivo* experiments, an increased  
229 proliferation of high-neural glioblastoma cells but not low-neural glioblastoma cells was seen  
230 when co-cultured with neurons ( $p < 0.001$ , Fig. 4m-n). Furthermore, we found an increase of  
231 co-localization of synapse puncta in high-neural glioblastoma cells ( $p < 0.001$ , Fig 4o),  
232 supporting the previously mentioned findings after xenografting. Since neuronal activity has  
233 recently been shown to be a factor in widespread infiltration of glioblastoma cells<sup>15</sup>, we  
234 wondered if this was also a characteristic of the high-neural glioblastomas in our study. For  
235 this purpose, we performed a migration assay, in which a significantly wider migration of high-  
236 neural glioblastoma cells could be demonstrated ( $p < 0.05$ , Fig. 4p).

237 The translation of the neural signature into cell cultures and PDX models demonstrates the  
238 robustness of the epigenetically imprinted neural signature and indicates its distinct role within  
239 neuron-to-glioma networks of the high-neural glioblastoma subgroup.

240

241 ***High neural glioblastoma shows increased tumor connectivity and remains***  
242 ***spatiotemporally stable***

243 Previous studies have reported a relationship between tumor connectivity and patient  
244 survival<sup>10,25</sup>. Here, we measured functional tumor connectivity using  
245 magnetoencephalography (n = 38, Fig. 5a-b) and resting state functional magnetic resonance  
246 imaging (n = 44, Fig. 5c-e) in glioblastoma patients. Both modalities showed a significant  
247 association of higher connectivity with the high-neural subgroup (p < 0.01, Fig. 5a-e). These  
248 findings are consistent with a recent study of distinct cellular states in regions of HFC-  
249 glioblastoma<sup>10</sup>. Comparing the functional connectivity phenotype<sup>10</sup> to our neural classification,  
250 we found high concordance between both classifications. Volumetric analysis showed  
251 significantly smaller volumes of contrast-enhancement (p = 0.03, Fig. 5f) in high-neural  
252 glioblastoma, but no association with fluid attenuated inversion recovery (FLAIR) signal  
253 abnormality volume (p = 0.18, Fig. 5g) and necrotic volume (p = 0.78, Fig. 5h).

254

255 To address the topic of spatiotemporal heterogeneity, we analyzed spatially collected biopsies  
256 (3 to 7 samples of 34 patients, n = 143). Among them, 23 patients (67.6%) had a pure low- or  
257 high-neural signature, and a predominant signature was present in an additional 10 patients  
258 (29.4%) (Fig. 5i). To describe temporal stability, neural signatures were analyzed in 39 patients  
259 with matched tissue obtained from first and recurrence surgery (Fig. 5j-k). Here, 31 of 39  
260 patients (79.5%) were categorized in the same neural subgroup at recurrence as at the time  
261 of diagnosis (Fig. 5k). Overall, the neural subgroup appeared to be spatiotemporally stable, in  
262 contrast to transcriptional states that change in a larger proportion of patients<sup>14,26</sup>.

263

264

## 265 ***Drug sensitivity analysis of neural glioblastoma cells***

266 Glioblastoma patients routinely undergo combined radio-chemotherapy after surgical  
267 resection<sup>27</sup>. We therefore evaluated 27 different agents for their efficacy in the treatment of  
268 low- and high-neural glioblastoma cells (Supplementary Fig. 6a). We observed a trend for  
269 increased cleaved caspase 3 (Supplementary Fig. 6b) and reduced tumor cell size  
270 (Supplementary Fig. 6c) after treatment with lomustine (CCNU), JNJ10198400, and  
271 cyclosporine-treated high-neural glioblastoma cells, whereas talazoparib showed a trend for  
272 greater sensitivity in low-neural glioblastoma cells. However, none of these compounds  
273 reached statistical significance (Supplementary Fig. 6d). Therefore, we wondered about the  
274 prognostic impact of surgical resection in low- and high-neural glioblastoma since surgery is  
275 a cornerstone of glioblastoma therapy, and we previously demonstrated survival differences  
276 for other methylation-based glioblastoma subclasses<sup>28</sup>.

277

## 278 ***Neural classification predicts benefit of resection in glioblastoma***

279 Glioblastomas are epigenetically assigned to different subclasses with *receptor tyrosine*  
280 *kinase (RTK) I, RTK II* and mesenchymal (MES) being the most prominent in adult patients<sup>29</sup>.  
281 Here, *RTK I* and *RTK II* tumors showed a comparable neural signature while MES tumors had  
282 the lowest neural signature (Fig. 6a). Given the different neural signatures between  
283 methylation-based subclasses, we hypothesized that the neural signature might constitute a  
284 factor for determining benefit from different categories of extent of resection (EOR). In low-  
285 neural glioblastoma, a significant survival benefit of gross total resection (GTR) (100% CE  
286 resection) and near-GTR ( $\geq 90\%$  CE resection) was observed compared with partial resection  
287 (PR;  $< 90\%$  CE resection) ( $p < 0.001$ , Fig. 6b). In contrast, the survival benefit of a near-GTR  
288 was not seen in high-neural glioblastoma (Fig. 6c). To further validate the differential benefit  
289 at distinct extents of resection in the two neural subgroups, we applied the current criteria of  
290 the Response Assessment in Neuro-Oncology (RANO) resection group<sup>30</sup> to a subset of 174  
291 glioblastomas from our clinical cohort.

292 Here, again, it was found that the benefit of the category for extent of resection depends on  
293 the neural subgroup (Supplementary Fig. 7). While an extent of resection of category 3A ( $\leq$   
294 5cm CE) showed a significant survival benefit in patients with a low-neural glioblastoma  
295 compared to category 3B ( $\geq$  5cm CE), this was not evident in the high-neural tumors  
296 (Supplementary Fig. 7). Consideration of the *MGMT* promoter showed a survival benefit of a  
297 methylated promoter in both subgroups, but a striking difference in low-neural glioblastoma  
298 with a median OS difference of 12.0 months depending on the *MGMT* promoter methylation  
299 status ( $p < 0.0001$ , Fig. 6d). Our combined survival data demonstrate that glioblastomas with  
300 a high-neural signature have an unfavorable survival prognosis, and a greater resection of  
301 contrast-enhancing tumor areas may be required to achieve a survival benefit in this distinct  
302 glioblastoma subclass.

303

### 304 ***Serum biomarkers of high-neural glioblastoma***

305 Further, we investigated whether preoperative assessment of the neural subgroup is feasible  
306 in blood. For this purpose, we determined the neural signature of circulating DNA analytes  
307 (extracellular vesicles (EV)-associated DNA and cell-free DNA (cfDNA)) in plasma of  
308 glioblastoma patients (Fig. 6e-f). Healthy individuals and meningioma patients were used as  
309 controls. Circulating EVs, a known blood-derived surrogate marker for tumor presence in  
310 glioblastoma<sup>31</sup> and involved in neuron-to-glioma synchronization<sup>32</sup>, correlated with the neural  
311 signature of the distant glioblastoma ( $p < 0.01$ ,  $n=55$ , Fig. 6e). Epigenetic profiling of EV-DNA  
312 in plasma showed a detectable neural signature that was not evident in cfDNA (Fig. 6f).  
313 Additionally, the neural signature in EV-DNA was significantly increased in glioblastoma  
314 compared to the two control groups (Fig. 6f). Apart from the detection of the neural signature  
315 in patient serum, brain-derived neurotrophic factor (BDNF) was repeatedly demonstrated as  
316 one factor for promoting neuronal activity-regulated glioma growth and reinforcing neuron-to-  
317 glioma interactions<sup>4,33</sup>. We determined BDNF serum levels from 94 glioblastoma patients at  
318 time of diagnosis (Fig. 6g-h).

319 Patients with high-neural glioblastoma exhibited elevated BDNF serum levels compared to  
320 low-neural glioblastoma as well as meningioma (n=13) and healthy donors (n=19) (Fig. 6g).  
321 Glioblastomas with higher BDNF serum levels had a decreased immune cell signature,  
322 consistent with the low immune cell signature of high-neural tumor tissue samples (Fig. 6i).  
323 Since neuronal activity increased BDNF release and current literature describes BDNF  
324 elevation in serum after provoked seizures for electroconvulsive therapy<sup>34,35</sup>, we hypothesized  
325 that tumor-associated epilepsy may also promote BDNF release. Here, we observed a  
326 significant increase of BDNF levels in patients with epileptic seizures at time of diagnosis ( $p =$   
327  $0.02$ , Fig. 6j) and during follow-up ( $p < 0.001$ , Fig. 6k).  
328 These data suggest that EV-DNA and BDNF may serve as serum markers to stratify  
329 glioblastoma patients according to their neural subgroup and can be utilized for potential future  
330 targeted therapies.

331

332 ***Epigenetic neural classification informs patients survival in H3 K27-altered***  
333 ***diffuse midline glioma***

334 Besides glioblastoma, the importance of neuronal activity in promoting tumor growth in DMG  
335 has been highlighted in previous studies<sup>4,5</sup>. Therefore, we aimed to identify the neural  
336 signature in an additional cohort of H3 K27-altered DMG. The cohort consisted of patients  
337 from our institutional cohort (n=21), Chen et al.<sup>36</sup> (n=24), and Sturm et al.<sup>29</sup> (n=10). The neural  
338 signature was evenly distributed among tumors in the thalamus, pons, and medulla  
339 (Supplementary Fig. 8a). As previously observed for glioblastomas, CpG sites within the  
340 genes associated with invasivity, neuron-to-glioma synapse formation, and transsynaptic  
341 signaling were predominantly hypomethylated in high-neural DMG (Supplementary Fig. 8b).  
342 Additionally, cell state composition analysis showed a higher immune component in low neural  
343 tumors, whereas high-neural DMG samples were associated with stem and glial cell states  
344 (Supplementary Fig. 8c). Further, the malignant stem cell-like, OPC-like state was found to be  
345 correlated with synaptic gene expression in a single-cell RNAseq dataset by Venkatesh and

346 colleagues ( $p = 0.01$ ,  $r^2 = 0.40$ , Supplementary Fig. 8d)<sup>3</sup>. Survival analysis of 72 pediatric and  
347 adolescent patients showed an unfavorable outcome for high-neural DMG ( $p < 0.01$ ,  
348 Supplementary Fig. 8e). The survival difference between low- and high-neural DMG was  
349 significant when localized in the thalamus ( $p < 0.01$ , Supplementary Fig. 8f) but not in the pons  
350 ( $p = 0.08$ , Supplementary Fig. 8h) and medulla ( $p = 0.32$ , Supplementary Fig. 8g).  
351 These results for patients with a DMG are consistent with the previous findings in glioblastoma  
352 and confirm the relevance of the neural signature in an additional type of IDH-wildtype high-  
353 grade glioma.

## 354 **DISCUSSION**

355 In recent years, the bidirectional interaction between glioma cells and neural cells, with their  
356 ability to form synapses and integrate into neuronal circuits, has been identified as a major  
357 factor in oncogenesis and tumor progression<sup>3,4,13,37</sup>. In this study, we identified an  
358 epigenetically defined malignant neural signature as a potential marker for neural-to-glioma  
359 interactions among glioblastoma and DMG and present the following findings: 1. A malignant  
360 neural signature is increased in glioblastoma and DMG, compared with non-malignant brain  
361 tumors. 2. High-neural glioblastoma confers an unfavorable survival in humans and mice, and  
362 in addition, the neural signature is associated with higher functional connectivity in  
363 glioblastoma patients. 3. High-neural glioblastoma shows an increased malignant stem cell  
364 and NPC/OPC-like character but decreased immune infiltration. 4. The neural signature  
365 remains robust in PDX mouse models and high-neural glioblastoma bearing mice show higher  
366 proliferation and migration as well as increased neuron-to-glioma synapses. 5. High-neural  
367 tumors benefit from a maximized resection. 6. The epigenetic neural signature can be detected  
368 in circulating EVs. 7. Elevated BDNF serum levels are present in high-neural glioblastoma and  
369 are associated with a higher rate of preoperative and therapy-refractory seizures. 8. The  
370 neural signature and its prognostic value can also be seen in DMG, an additional IDH-wildtype  
371 malignant glioma tumor type.

372

373 Gliomas encompass a variety of cellular components of the tumor microenvironment, and  
374 subgroups can be described according to distinct cellular states<sup>38</sup>. In addition, epigenome  
375 profiling and deconvolution were shown to characterize the microenvironment of glioma  
376 methylation subclasses<sup>39,40</sup>. We further distinguished IDH-wildtype gliomas according to their  
377 epigenetic neural signature as a potential marker of neuron-to-glioma interactions. An  
378 increase in neural signature was found in glioblastoma and DMG, which reflects the findings  
379 of previous studies in preclinical models<sup>3,5</sup>.

380 By multi-dimensional profiling, high-neural glioblastoma showed upregulation and  
381 hypomethylation of genes known to be associated with invasiveness and neuron-to-glioma  
382 synapse formation and signaling. It is well established that glioma growth occurs through  
383 paracrine signaling and glutamatergic synaptic input<sup>3-6,33</sup>, and recently Venkataramani and  
384 colleagues subdivided glioblastoma cells into unconnected and connected cells with unique  
385 cell states, explaining brain infiltration through hijacking of neuronal mechanisms<sup>13</sup>. Spatial  
386 transcriptomic analysis revealed a malignant OPC/NPC-like character of high-neural  
387 glioblastoma cells consistent with the unconnected glioblastoma cells described by  
388 Venkataramani that hijack neuronal mechanisms and drive brain invasion. Additional cell state  
389 composition analysis profiled these high-neural tumors with a malignant stem cell-like  
390 character. Of note, the observed diploid oligodendrocyte transcriptomic module may represent  
391 a tumor cell population of primary near-diploid state as glioblastomas are karyotypically  
392 heterogeneous tumors, composed of many cellular populations<sup>41</sup>.

393

394 The clinical relevance of our findings is supported by the observation that patients suffering  
395 from high-neural glioblastoma or DMG had an unfavorable overall and progression-free  
396 survival. In addition, a greater extent of resection must be achieved to have prognostic  
397 improvement in high-neural glioblastoma, which may explain the results of our previous study  
398 examining the impact of DNA methylation subclasses<sup>28</sup>. Our findings are in line with a recent  
399 study by Krishna and colleagues which also showed poorer survival in patients with  
400 glioblastoma that exhibited high functional connectivity.<sup>10</sup> Translating our signature to samples  
401 from Krishna et al. related an increased functional connectivity to a higher neural signature.  
402 The findings of this translational approach between both studies highlights *TSP-1*, a crucial  
403 driver of functional connectivity identified in Krishna's study, as a potential therapeutic target.  
404 To further address the importance of tumor connectivity, we integrated glioblastoma patients  
405 who underwent preoperative resting state functional MRI and could also find an increased  
406 connectivity of high-neural glioblastomas to its peritumoral surrounding.



407 The synaptogenic character with increased functional connectivity of high-neural  
408 glioblastomas could be replicated with *in vivo* and *in vitro* experiments. Collectively, these data  
409 underscore the tremendous importance of the synaptic integration of gliomas into neuronal  
410 circuits and targeting these neuron-to-glioma networks appears to be a promising therapeutic  
411 approach.<sup>1,12</sup>

412

413 One factor raising attention is *BDNF*, a neuronal activity-regulated neurotrophin, which has  
414 been found to promote glioma growth<sup>4,42</sup>. Taylor et al. characterized BDNF as an enhancer of  
415 neural-glioma interactions and demonstrated therapeutic potential of interrupting BDNF-TrkB  
416 signaling in pediatric IDH-wildtype glioblastoma and DIPG<sup>33</sup>. Here, we found elevated serum  
417 BDNF levels in adult patients with a high-neural glioblastoma. Potential sources of elevated  
418 BDNF include neurons in a glioma-induced state of hyperexcitability<sup>3</sup>, given the known activity-  
419 regulation of BDNF expression and secretion<sup>43-45</sup> or possibly from glioblastoma cells, as a  
420 subset of glioblastoma cells express and secrete BDNF<sup>46</sup>. Additionally, and consistent with  
421 findings in preclinical models, elevated serum BDNF levels were associated with a higher  
422 seizure frequency. The relationship between BDNF and seizure outcome fits with previously  
423 published data, as on the one hand BDNF regulates trafficking of *AMPA* to the postsynaptic  
424 membrane of glioma<sup>33</sup> and on the other hand an upregulation and hypomethylation of *AMPA*  
425 genes was found in the *RTK II* subclass, a highly epileptogenic glioblastoma subclass<sup>47,48</sup>.  
426 Here, neuronal activity arising from glioma-to-neuron interactions during tumor growth or the  
427 onset of seizures seems to be a pivotal driver for BDNF release, as increased BDNF serum  
428 concentrations have already been shown after artificial induction of activity by  
429 electroconvulsive therapy.<sup>34,35</sup> Briefly summarized, these results identify a biomarker of high-  
430 neural glioblastoma, underline the importance of BDNF in glioma progression as well as  
431 tumor-related epilepsy, and highlight disruption of BDNF-TrkB signaling as a therapeutic  
432 target.

433

434 While this axis may represent a therapeutic target for high-neural glioblastoma, we further  
435 identified low-neural tumors as immune-enriched based on transcriptomic and cell state  
436 composition analysis. Consequently, one could hypothesize that two opposing glioblastoma  
437 subtypes appear to be differentiated here and will need to be pursued in future studies and  
438 therapeutic avenues. The identification of an immunosuppressive state in high-neural  
439 glioblastoma is concordant with recent findings by Nejo et al. who described  
440 immunosuppressive mechanisms in thrombospondin-1-upregulated glioma samples<sup>49</sup>. Taken  
441 together, stratification of IDH-wildtype gliomas based on their epigenetic neural signature may  
442 provide a potential tool for predicting response to neuroscience-guided therapies.  
443

## 444 **Conclusion**

445 Overall, the definition of a high-neural signature in IDH-wildtype glioma revealed an OPC- and  
446 NPC-like character with a malignant stem cell-like state that affects patient survival, remains  
447 stable during therapy, and is conserved in preclinical models. This knowledge supports  
448 clinicians in stratifying glioma patients according to their prognosis and determining the  
449 surgical and neuro-oncological benefit for current standard of care. Lastly, the here presented  
450 clinical translation in the field of glioma neuroscience using an epigenetic neural signature  
451 may advance the development of trials with neuroscience-guided therapies.

452

## 453 **METHODS**

### 454 ***DNA Methylation Profiling***

455 DNA was extracted from tumors, extracellular vesicles, and bulk plasma, and analyzed for  
456 genome-wide DNA methylation patterns using the Illumina EPIC (850k) array. Processing of  
457 DNA methylation data was performed with custom approaches.<sup>50</sup> Methylation profiling results  
458 from first surgery were submitted to the molecular neuropathology (MNP) methylation  
459 classifier v12.5 hosted by the German Cancer Research Center (DKFZ).<sup>17</sup> Patients were  
460 included if the calibrated score for the specific methylation class was  $>0.84$  at time of diagnosis  
461 in accordance with recommendations by Capper et al.<sup>50</sup> For *IDH*-wildtype glioblastoma,  
462 patients with a score below 0.84 but above 0.7 with a combined gain of chromosome 7 and  
463 loss of chromosome 10 or amplification of epidermal growth factor receptor (*EGFR*) were  
464 included in accordance with cIMPACT-NOW criteria.<sup>51</sup> Furthermore, a class member score of  
465  $\geq 0.5$  for one of the glioblastoma subclasses was required. Evaluation of the *MGMT* promoter  
466 methylation status was made from the classifier output v12.5 using the *MGMT*-STP27  
467 method.<sup>52</sup>

468

### 469 ***Processing of Methylation Arrays***

470 All idats corresponding to methylation array data were processed similarly using the minfi  
471 package in R (version 1.40.0).<sup>53</sup> The data was processed using the preprocessIllumina  
472 function. Only probes with detection p-values  $<0.01$  were kept for further analysis. Also,  
473 probes with  $<3$  beads in at least 5% of samples, as well as all non-CpG probes, SNP-related  
474 probes, and probes located on X and Y chromosomes were discarded. The CpG intensities  
475 were converted into beta values representing total methylation levels (between 0 and 1).

476

477

478

479

## 480 ***Cell Type Deconvolution***

481 Non-negative least square (NNLS) linear regression was used in deconvolving the beta values  
482 of methylation arrays into cell type components.<sup>16,54,55</sup> As a reference, a publicly available  
483 signature was obtained from Moss et al. (2018) consisting of gene expressions for 25 cell type  
484 components (Monocytes\_EPIC, B-cells\_EPIC, CD4T-cells\_EPIC, NK-cells\_EPIC, CD8T-  
485 cells\_EPIC, Neutrophils\_EPIC, Erythrocyte\_progenitors, Adipocytes, Cortical\_neurons,  
486 Hepatocytes, Lung\_cells, Pancreatic\_beta\_cells, Pancreatic\_acinar\_cells,  
487 Pancreatic\_duct\_cells, Vascular\_endothelial\_cells, Colon\_epithelial\_cells, Left\_atrium,  
488 Bladder, Breast, Head\_and\_neck\_larynx, Kidney, Prostate, Thyroid, Upper\_GI,  
489 Uterus\_cervix) and 6,105 unique CpGs.<sup>16</sup>

490

## 491 ***Integrative Analysis of Methylation and Gene Expression***

492 The analysis of gene expression co-correlation networks was conducted using Weighted  
493 Correlation Network Analysis (WGCNA)<sup>56</sup>, in which the epigenetic Moss-signature was  
494 incorporated as trait features. Initially, we calculated the optimal soft power to achieve a scale-  
495 free topology. This was done by fitting a model for different soft power thresholds (ranging  
496 from 1 to 20), with an optimal power of 16. Following this, a signed co-expression network was  
497 created utilizing the Topological Overlap Matrix (TOM)<sup>57</sup> via the hdWGCNA's  
498 ConstructNetwork function<sup>58</sup>. For dimension reduction and visualization of the co-expression  
499 network, we employed the Uniform Manifold Approximation and Projection (UMAP) via the  
500 ModuleUMAPPlot function. We then identified the hub genes within each module by  
501 calculating module connectivity using the ModuleConnectivity function. Gene ontology  
502 analysis was subsequently performed on the top 100 module-associated genes using the  
503 compareCluster function. Visualization of module-associated pathway activations was  
504 accomplished using the clusterProfiler package<sup>59</sup>, specifically via the dotplot function.

505

506

## 507 ***Single Cell Data Analysis***

508 To contextualize the gene expression modules significantly associated with the low-/ high-  
509 neural epigenetic phenotype, we computed eigengene signatures and examined their  
510 expression patterns using the GBMap single-cell reference dataset<sup>60</sup>. We downloaded and  
511 processed GBMap using the Seurat package. The AddModuleScore function of the Seurat  
512 package was used to compute the module eigengene score for each cell. For visualization,  
513 we projected the model expression onto the cell-level UMAP (Uniform Manifold Approximation  
514 and Projection) provided by GBMap's integration algorithm.

515

## 516 ***Spatially Resolved Transcriptomics Data Analysis***

517 We accessed spatial transcriptomic data from our institute recently published<sup>20</sup> and  
518 preprocessed the corresponding EPIC methylation data by the pipeline above. Computational  
519 analysis was employed by the SPATA2 package (v2.01). For spatial projection of the module  
520 eigengene signatures, we used the joinWithGenes function and averaged the expression  
521 across all genes. Spatial surface plots were performed by the plotSurface function without  
522 smoothing. Spatial correlation analysis was performed by the MERINGUE package<sup>61</sup> using  
523 the spatial cross correlation analysis. Spatial proximity analysis, we performed a correlation-  
524 based analysis using low- or high-neural glioblastoma samples. A spatial correlation matrix  
525 was generated using SPATA2's joinWithFeatures function, which incorporates the  
526 annotation\_level\_4 data from the GBMap single cell deconvolution. The correlation matrices  
527 were then averaged using the Reduce function. To estimate the average cellular abundance  
528 of each cell type/state, we employed a similar approach. The resulting correlation matrix was  
529 transformed into a distance matrix, with correlation values subtracted from 1. We then applied  
530 a threshold, setting distances derived from correlations less than 0.5 to zero, effectively  
531 removing low correlation connections. Subsequently, we created a graph object from the  
532 distance matrix using the graph\_from\_adjacency\_matrix function from the igraph package<sup>62</sup>.  
533 We added attribute data (cell type and abundance) to the graph vertices.

534 Next, we computed a minimum spanning tree from the graph to simplify and highlight the core  
535 structure of the network. Edge weights were normalized to a range between 0.5 and 2, setting  
536 the basis for edge width in subsequent graph visualization. Finally, we visualized the graph  
537 using the ggraph package<sup>63</sup>, incorporating edge links and node points, which were color-coded  
538 and sized according to cellular abundance. Node labels were added with the geom\_node\_text  
539 function and repelled for better visibility.

540

### 541 ***Cell State Composition Analysis***

542 To infer the abundance of cell type and cell state in the samples, we subjected each sample  
543 to bulk DNA methylation assay using EPIC arrays and applied the Silverbush et al.  
544 deconvolution method<sup>64</sup>. The deconvolution method is a reference free method that uses a  
545 hierarchical matrix factorization approach inferring both cell types and the cell states therein.  
546 The method was trained on the DKFZ glioblastoma cohort and tested on TCGA glioblastoma  
547 cohort and was able to infer the abundance of cell types in the microenvironment (immune,  
548 glia and neuron) and malignant cell states (malignant stem-like cells component and two  
549 differentiated cells components). We applied the method as described in Silverbush et al.  
550 using the cell type and cell state encoding provided in the manuscript and via the engine  
551 provided in EpiDISH<sup>65</sup> package, with RPC method and maximum iterations of 2000.

552

### 553 ***DNA Tumor Purity***

554 Tumor-purity was calculated using the RF\_purify Package in R.<sup>66</sup> This package uses the  
555 “absolute” method which measures the frequency of somatic mutations within the tumor  
556 sample and relates this to the entire DNA quantity.<sup>67</sup>

557

558

559

560

## 561 ***Isolation and Analysis of Extracellular Vesicles (EVs)***

562 EVs were isolated from plasma of glioblastoma patients by differential centrifugation as  
563 previously described.<sup>31,68</sup> Plasma and culture supernatants were centrifuged at 300 x g for 5  
564 min to eliminate cells, followed by 2000 x g for 10 min to remove platelets and remaining cell  
565 debris. Thereafter, the cleared plasma and supernatants were centrifuged at 10,000 x g for 30  
566 min (4°C) to remove large vesicles, and then followed to ultracentrifugation at 100,000 x g for  
567 70 min (4°C), where EV pellets were resuspended with 0.22µm-filtered (Millipore) PBS. The  
568 concentration and size of EVs were determined by nanoparticle tracking analysis (NTA), using  
569 an LM14 instrument (NanoSight, Malvern Panalytical) equipped with a 638 nm laser and a  
570 Merlin F-033B IRF camera (Adept Electronic Solutions). EV-enriched samples were diluted  
571 1:300 in PBS prior to NTA. Triple movies (30 seconds each) were recorded on camera level  
572 15, and then analyzed with detection threshold 6 in NTA 3.2 Build 16. As routine, EVs were  
573 also characterized according to size and morphology by electron microscopy, and according  
574 to EV markers (CD9, CD63, CD81) by Imaging Flow Cytometry (data not shown). DNA was  
575 extracted from EVs using the MasterPure Complete DNA and RNA Purification Kit (Biosearch  
576 Technologies). For comparison purposes, bulk cfDNA was isolated from plasma with the  
577 MagMax™ cfDNA Isolation Kit (Applied Biosystems).

578

## 579 ***Detection of BDNF Serum Levels***

580 Plasma from glioblastoma patients was isolated by double spin centrifugation of whole blood.  
581 Samples were aliquoted and stored at -80 C before use. BDNF plasma levels were detected  
582 using the LEGENDplex Neuroinflammation Panel 1 (Biolegend, San Diego, CA, USA). Data  
583 was acquired using the BD LSR Fortessa and Beckman Coulter Cytoflex LX flow cytometer  
584 and analyzed with the BioLegend LEGENDplex software.

585

586

587



## 588 ***Proteomic Processing of Human Glioblastoma Samples***

589 FFPE samples of tumors were obtained from tissue archives from the neuropathology unit  
590 in Hamburg. Tumor samples were fixed in 4 % paraformaldehyde, dehydrated, embedded in  
591 paraffin, and sectioned at 10 µm for microdissection using standard laboratory protocols. For  
592 paraffin removal FFPE tissue sections were incubated in 0.5 mL n-heptane at room  
593 temperature for 30 min, using a ThermoMixer (ThermoMixer® 5436, Eppendorf). Samples  
594 were centrifuged at 14.000 g for 5 min and the supernatant was discarded. Samples were  
595 reconditioned with 70% ethanol and centrifuged at 14.000 g for 5 min. The supernatant was  
596 discarded. The procedure was repeated twice. Pellets were dissolved in 150 µL 1 % w/v  
597 sodium deoxycholate (SDC) in 0.1 M triethylammonium bicarbonate buffer (TEAB) and  
598 incubated for 1 h at 95 °C for reverse formalin fixation. Samples were sonicated for 5 seconds  
599 at an energy of 25% to destroy interfering DNA. A bicinchoninic acid (BCA) assay was  
600 performed (Pierce™ BCA Protein Assay Kit, Thermo Scientific) to determine the protein  
601 concentration, following the manufacturer's instructions. Tryptic digestion was performed for  
602 20 µg protein, using the Single-pot, solid-phase-enhanced sample preparation (SP3)  
603 protocol<sup>69</sup>. Eluted Peptides were dried in a Savant SpeedVac Vacuumconcentrator (Thermo  
604 Fisher Scientific, Waltham, USA) and stored at -20° until further use. Directly prior to  
605 measurement dried peptides were resolved in 0.1% FA to a final concentration of 1 µg/µl. In  
606 total 1 µg was subjected to mass spectrometric analysis.

607

## 608 ***Liquid Chromatography–Tandem Mass Spectrometer Parameters***

609 Liquid chromatography–tandem mass spectrometer (LC–MS/MS) measurements were  
610 performed on a quadrupole-ion-trap-orbitrap mass spectrometer (MS, QExactive, Thermo  
611 Fisher Scientific, Waltham, MA, USA) coupled to a nano-UPLC (Dionex Ultimate 3000 UPLC  
612 system, Thermo Fisher Scientific, Waltham, MA, USA). Tryptic peptides were injected to the  
613 LC system via an autosampler, purified and desalted by using a reversed phase trapping  
614 column (Acclaim PepMap 100 C18 trap; 100 µm × 2 cm, 100 Å pore size, 5 µm particle size;

615 Thermo Fisher Scientific, Waltham, MA, USA), and thereafter separated with a reversed phase  
616 column (Acclaim PepMap 100 C18; 75  $\mu\text{m}$   $\times$  25 cm, 100 Å pore size, 2  $\mu\text{m}$  particle size,  
617 Thermo Fisher Scientific, Waltham, MA, USA). Trapping was performed for 5 min at a flow  
618 rate of 5  $\mu\text{L}/\text{min}$  with 98% solvent A (0.1% FA) and 2% solvent B (0.1% FA in ACN). Separation  
619 and elution of peptides were achieved by a linear gradient from 2 to 30% solvent B in 65 min  
620 at a flow rate of 0.3  $\mu\text{L}/\text{min}$ . Eluting peptides were ionized using a nano-electrospray ionization  
621 source (nano-ESI) with a spray voltage of 1800 V, transferred into the MS, and analyzed in  
622 data dependent acquisition (DDA) mode. For each MS1 scan, ions were accumulated for a  
623 maximum of 240 ms or until a charge density of  $1 \times 10^6$  ions (AGC target) were reached.  
624 Fourier-transformation-based mass analysis of the data from the orbitrap mass analyzer was  
625 performed by covering a mass range of 400–1200  $m/z$  with a resolution of 70,000 at  $m/z =$   
626 200. Peptides with charge states between 2+–5+ above an intensity threshold of 5 000 were  
627 isolated within a 2.0  $m/z$  isolation window in top-speed mode for 3 s from each precursor scan  
628 and fragmented with a normalized collision energy of 25%, using higher energy collisional  
629 dissociation (HCD). MS2 scanning was performed, using an orbitrap mass analyzer, with a  
630 starting mass of 100  $m/z$  at an orbitrap resolution of 17,500 at  $m/z = 200$  and accumulated for  
631 50 ms or to an AGC target of  $1 \times 10^5$ . Already fragmented peptides were excluded for 20 s.  
632

### 633 ***Proteomic Data Processing***

634 Proteomic samples ( $n=28$ ) were measured with liquid chromatography tandem mass  
635 spectrometry (LC-MS/MS) systems and processed with Proteome Discoverer 3.0. and  
636 searched against a reviewed FASTA database (UniProtKB: Swiss-Prot, Homo sapiens,  
637 February 2022, 20300 entries). To cope with protein injection amount differences, the protein  
638 abundances were normalized at the peptide level. Perseus 2.0.3 was used to obtain log2  
639 transformed intensities. The imputation was performed using the Random Forest imputation  
640 algorithm (Hyperparameters: 1000 Trees and 10 repetitions) in RStudio 4.3.

641

## 642 **Weighted Correlation Network Analysis (WGCNA)**

643 The WGCNA package in R (version 1.70.3) was used to identify gene co-expression gene  
644 modules.<sup>56</sup> The minimum module size was set to 10 and a merging threshold of 0.40 was  
645 defined. Based on the assessment of scale-free topology, soft-power of 9 was selected. To  
646 construct modules, we first corrected for any technical batch effect using Empirical Bayes-  
647 moderated adjustment using empiricalBayesLM function of WGCNA. Modules were assessed  
648 based on their correlation with traits (low and high) and their levels of significance (associated  
649 with two-tailed Student's t-test). The significant modules ( $p < 0.05$ ) were used for further  
650 analysis. All genesets within a module were used for overrepresentation analysis using  
651 clusterProfiler package<sup>59</sup> in R (Version 4.2.0). Further to identify cell type enrichment within  
652 each module, gene-sets from PanglaoDB3 were used through enrichr in python (Package  
653 maayanlab\_bioinformatics, version 0.5.4)<sup>70</sup>. To assess the module scores on single-cells,  
654 Scanpy's score\_genes function was used to calculate module scores using core glioblastoma  
655 single-cell atlas<sup>60</sup>.

656

## 657 **Mice Housing**

658 *In vivo* experiments were conducted in accordance with protocols approved by the Stanford  
659 University Institutional Animal Care and Use Committee (IACUC) as well as the University  
660 Medical Center Hamburg-Eppendorf (Hamburg, Germany). Experiments were performed in  
661 accordance with institutional guidelines and explicit permission from the local authorities  
662 (Behörde für Soziales, Gesundheit und Verbraucherschutz Hamburg, Germany). Animals  
663 were housed according to standard guidelines under pathogen-free conditions, in  
664 temperature- and humidity-controlled housing with free access to food and water in a 12 h  
665 light:12 h dark cycle. For brain tumor xenograft experiments, the IACUC does not set a limit  
666 on maximal tumor volume but rather on indications of morbidity. In no experiments were these  
667 limits exceeded as mice were euthanized if they exhibited signs of neurological morbidity or if  
668 they lost 15% or more of their body weight.

669 ***Orthotopic Xenografting of Patient-Derived Low- and High-Neural Glioblastoma***

670 ***Cells***

671 For xenograft studies as presented in Fig. 4g-m, NSG mice (NOD-SCID-IL2R gamma chain-  
672 deficient, The Jackson Laboratory) were used, and experiments were performed at the  
673 Stanford University (United States). Male and female mice were used equally. A single-cell  
674 suspension from cultured primary patient-derived low- (“UCSF-UKE-1”) or high-neural  
675 (“UCSF-UKE-2”) glioblastoma neurospheres was prepared in sterile HBSS immediately  
676 before the xenograft procedure. Mice at postnatal day (P) 28–30 were anaesthetized with 1–  
677 4% isoflurane and placed in a stereotactic apparatus. The cranium was exposed through  
678 midline incision under aseptic conditions. Approximately 150,000 cells in 3  $\mu$ l sterile HBSS  
679 were stereotactically implanted into the premotor cortex (M2) through a 26-gauge burr hole,  
680 using a digital pump at infusion rate of 1.0  $\mu$ l min<sup>-1</sup>. Stereotactic coordinates used were as  
681 follows: 0.5 mm lateral to midline, 1.0 mm anterior to bregma, -1.0 mm deep to cortical  
682 surface.

683

684 Mice survival data from the orthotopic xenografts demonstrated in Fig. 4e were performed on  
685 NMRI-Foxn1nu immunodeficient mice (Janvier-Labs) and conducted at the University Medical  
686 Center Hamburg-Eppendorf (Germany). After dissociation, neurospheres from cultured  
687 primary patient-derived low- (“GS-8”, “GS-10”, “GS-73”, and “GS-80”) or high-neural (“GS-57”,  
688 “GS-74”, “GS-75”, “GS-101”) glioblastoma were resuspended in a concentration of 100.000  
689 cells/ $\mu$ l in HBSS and 2 $\mu$ l was injected in the striatum at the following stereotactic coordinates  
690 as follows: 2.0mm lateral to Bregma, 1.0mm anterior to Bregma, and -2.8mm deep to cortical  
691 surface. Cells were implanted using a Hamilton syringe with a 30-gauge needle. Further data  
692 is available in extended data 5.

693

694

695

## 696 ***Perfusion and Immunofluorescence Staining***

697 Eight weeks after xenograft, low and high neural glioblastoma-bearing mice were  
698 anaesthetized with intraperitoneal avertin (tribromoethanol), then transcardially perfused with  
699 20 ml of PBS. Brains were fixed in 4% PFA overnight at 4 °C, then transferred to 30% sucrose  
700 for cryoprotection for 48 h. Brains were then embedded in Tissue-Tek O.C.T. (Sakura) and  
701 sectioned in the coronal plane at 40 µm using a sliding microtome (Microm HM450; Thermo  
702 Scientific). For immunofluorescence, coronal sections were incubated in blocking solution (3%  
703 normal donkey serum, 0.3% Triton X-100 in TBS) at room temperature for 30 min. Mouse anti-  
704 human nuclei clone 235-1 (1:100; Millipore), rabbit anti-Ki67 (1:500; Abcam ab15580), rat anti-  
705 MBP (1:200; Abcam ab7349), mouse anti-nestin (1:500; Abcam ab6320), guinea pig anti-  
706 synapsin1/2 (1:500; Synaptic Systems), chicken anti-neurofilament (M+H; 1:1000; Aves Labs)  
707 or PSD95 (1:500, Abcam ab18258), were diluted in antibody diluent solution (1% normal  
708 donkey serum in 0.3% Triton X-100 in TBS) and incubated overnight at 4 °C. Sections were  
709 then rinsed three times in TBS and incubated in secondary antibody solution (Alexa 488  
710 donkey anti-rabbit IgG; Alexa 594 donkey anti-mouse IgG, Alexa 647 donkey anti-chicken IgG,  
711 Alexa 405 donkey anti-guinea pig IgG, Alexa 647 donkey anti-rabbit IgG, or Alexa 594 donkey  
712 anti-mouse IgG all used at 1:500 (Jackson Immuno Research) in antibody diluent at 4 °C.  
713 Sections were rinsed three times in TBS and mounted with ProLong Gold Mounting medium  
714 (Life Technologies).

715

## 716 ***Confocal Imaging and Quantification of Cell Proliferation and Tumor Burden***

717 Cell quantification within xenografts was performed by a blinded investigator using live  
718 counting on a 20x objective of a Zeiss LSM900 scanning confocal microscope and Zen 3.7  
719 imaging software (Carl Zeiss). For overall tumor burden analysis, a 1-in-6 series of coronal  
720 brain sections were selected with 4 consecutive slices (4 fields per slice) at approximately 1.1–  
721 0.86 mm anterior to bregma analysed. Within each field, all HNA-positive tumor cells were  
722 quantified to determine tumor burden within the areas quantified. HNA-positive tumor cells

723 were then assessed for co-labelling with Ki67. To calculate the proliferation index (the  
724 percentage of proliferating tumor cells for each mouse), the total number of HNA-positive cells  
725 co-labelled with Ki67 across all areas quantified was divided by the total number of cells  
726 counted across all areas quantified (Ki67<sup>+</sup>/HNA<sup>+</sup>).

727

### 728 ***Confocal Puncta Quantification***

729 Images were collected using a 63×oil-immersion objective on a Zeiss LSM900 confocal  
730 microscope. Colocalization of all synaptic puncta images from low and high-neural  
731 glioblastoma xenograft samples described above were analyzed using a custom ImageJ  
732 processing script written at the Stanford Shriram Cell Science Imaging Facility to define each  
733 pre- and postsynaptic puncta and determine colocalization within a defined proximity of 1.5  
734 μM. To partially subtract local background, we used the ImageJ rolling ball background  
735 subtraction ([https://imagej.net/Rolling\\_Ball\\_Background\\_Subtraction](https://imagej.net/Rolling_Ball_Background_Subtraction)). The peaks were found  
736 using the `imglib2` `DogDetection` plugin  
737 ([https://github.com/imglib/imglib2algorithm/blob/master/src/main/java/](https://github.com/imglib/imglib2algorithm/blob/master/src/main/java/net/imglib2algorithm/dog/DogDetection.java)  
[net/imglib2/](https://github.com/imglib/imglib2algorithm/blob/master/src/main/java/net/imglib2algorithm/dog/DogDetection.java)  
[algorithm/dog/DogDetection.java](https://github.com/imglib/imglib2algorithm/blob/master/src/main/java/net/imglib2algorithm/dog/DogDetection.java)). In this plugin, the difference of Gaussians is used to  
739 enhance the signal of interest using two different sigmas: a 'smaller' sigma, which defines the  
740 smallest object to be found and a 'larger' sigma, for the largest object. The plugin then  
741 identifies the objects that are above the min peak value and assigns regions of interest (ROIs)  
742 to each channel. The number of neuron and glioma ROIs are counted, and the script extracts  
743 the number of glioma ROIs within 1.5μm of the neuron ROIs. This script was implemented in  
744 Fiji/ImageJ using the `ImgLib2` and `ImageJ Ops` ([https://imagej.net/ImageJ\\_Ops](https://imagej.net/ImageJ_Ops)) libraries.

745

746

747

748

749

## 750 ***Sample Preparation and Image Acquisition for Electron Microscopy***

751 Twelve weeks after xenografting of low- (n =3, “UCSF-UKE-1”) and high-neural glioblastoma  
752 cell (n = 3, “UCSF-UKE-2”), mice were euthanized by transcardial perfusion with Karnovsky’s  
753 fixative: 2% glutaraldehyde (EMS, 16000) and 4% PFA (EMS, 15700) in 0.1 M sodium  
754 cacodylate (EMS, 12300), pH 7.4. Transmission electron microscopy (TEM) was performed  
755 in the tumor mass within the CA1 region of the hippocampus for all xenograft analysis. The  
756 samples were then post-fixed in 1% osmium tetroxide (EMS, 19100) for 1 h at 4 °C, washed  
757 three times with ultrafiltered water, then en bloc stained overnight at 4 °C. The samples were  
758 dehydrated in graded ethanol (50%, 75% and 95%) for 15 min each at 4 °C; the samples were  
759 then allowed to equilibrate to room temperature and were rinsed in 100% ethanol twice,  
760 followed by acetonitrile for 15 min. The samples were infiltrated with EMbed-812 resin (EMS,  
761 14120) mixed 1:1 with acetonitrile for 2 h followed by 2:1 EMbed-812:acetonitrile overnight.  
762 The samples were then placed into EMbed-812 for 2 h, then placed into TAAB capsules filled  
763 with fresh resin, which were then placed into a 65 °C oven overnight. Sections were taken  
764 between 40 nm and 60 nm on a Leica Ultracut S (Leica) and mounted on 100-mesh Ni grids  
765 (EMS FCF100-Ni). For immunohistochemistry, microetching was done with 10% periodic acid  
766 and eluting of osmium with 10% sodium metaperiodate for 15 min at room temperature on  
767 parafilm. Grids were rinsed with water three times, followed by 0.5 M glycine quench, and then  
768 incubated in blocking solution (0.5% BSA, 0.5% ovalbumin in PBST) at room temperature for  
769 20 min. Primary goat anti-RFP (1: 300, ABIN6254205) was diluted in the same blocking  
770 solution and incubated overnight at 4 °C. The next day, grids were rinsed in PBS three times,  
771 and incubated in secondary antibodies (1:10 10 nm gold-conjugated IgG, TED Pella, 15796)  
772 for 1 h at room temperature and rinsed with PBST followed by water. For each staining set,  
773 samples that did not contain any RFP-expressing cells were stained simultaneously to control  
774 for any non-specific binding. Grids were contrast stained for 30 s in 3.5% uranyl acetate in  
775 50% acetone followed by staining in 0.2% lead citrate for 90 s. The samples were imaged

776 using a JEOL JEM-1400 TEM at 120 kV and images were collected using a Gatan Orius digital  
777 camera.

778

### 779 ***Electron Microscopy Data Analysis***

780 Sections from xenografted hippocampi of mice were imaged using TEM imaging. The  
781 xenografts were originally generated for a study by Krishna et al.<sup>10</sup> and mouse tissue was re-  
782 analyzed after epigenetic profiling and assignment to low- or high-neural glioblastoma groups.  
783 Here, 42 sections of high-neural glioblastoma across 3 mice and 45 sections of low-neural  
784 glioblastoma across 3 mice were analyzed. Electron microscopy images were taken at 6,000×  
785 with a field of view of 15.75  $\mu\text{m}^2$ . Glioma cells were counted and analyzed after identification  
786 of immunogold particle labelling with three or more particles. Furthermore, to determine  
787 synaptic structures all three of the following criteria had to be clearly met as previously  
788 described<sup>3</sup>: 1) presence of synaptic vesicle clusters, 2) visually apparent synaptic cleft, and 3)  
789 identification of postsynaptic density in the glioma cell. To quantify the percentage of glioma  
790 cells forming synaptic structures, the number of glioma-to-neuron synapses identified was  
791 divided by the total number of glioma cells analyzed.

792

### 793 ***Cell Culture***

794 Fresh glioblastoma samples were obtained from patients operated in the Department of  
795 Neurosurgery, University Medical Center Hamburg-Eppendorf (Germany). Samples were  
796 immediately placed in Hanks' balanced salt solution (HBSS, Invitrogen), transferred to the  
797 laboratory and processed within 20 min. The tissue was cut into  $<1 \text{ mm}^3$  fragments, washed  
798 with HBSS and digested with 1 mg/ml collagenase/dispase (Roche) for 30 min at 37 °C.  
799 Digested fragments were filtered using a 70  $\mu\text{m}$  cell mesh (Sigma-Aldrich), and the cells were  
800 seeded into T25 flasks at 2500–5000 cells/cm<sup>2</sup>. The culture medium consisted of neurobasal  
801 medium (Invitrogen) with B27 supplement (20  $\mu\text{l}/\text{ml}$ , Invitrogen), Glutamax (10  $\mu\text{l}/\text{ml}$ ,  
802 Invitrogen), fibroblast growth factor-2 (20 ng/ml, Peprotech), epidermal growth factor



803 (20 ng/ml, Peprotech) and heparin (32 IE/ml, Ratiopharm). Growth factors and heparin were  
804 renewed twice weekly. Spheres were split by mechanical dissociation when they reached a  
805 size of 200–500  $\mu\text{m}$ . In this study analyzed cell cultures with clinical data are represented in  
806 extended data 4. Long-term cultivation cell cultures were used from a publically available data  
807 set ( $n = 7$ , GSE181314) and one in house cell line ( $n = 1$ ).

808

### 809 ***Neuron-Glioma Co-Culture Experiments***

810 Neurons were isolated from CD1 (The Jackson Laboratory) mice at P0 using the Neural Tissue  
811 Dissociation Kit - Postnatal Neurons (Miltenyi), and followed by the Neuron Isolation Kit,  
812 Mouse (Miltenyi). After isolation, 150.000 neurons were plated onto glass coverslips (Electron  
813 Microscopy Services) after pre-treatment with poly-L-lysine (Sigma) and mouse laminin  
814 (Thermo Fisher) as described previously<sup>3</sup>. Neurons are cultured in BrainPhys neuronal  
815 medium (StemCell Technologies) containing B27 (Invitrogen), BDNF (10ng  $\text{ml}^{-1}$ ,  
816 Shenandoah), GDNF (5ng  $\text{ml}^{-1}$ , Shenandoah), TRO19622 (5 $\mu\text{M}$ ; Tocris),  $\beta$ - mercaptoethanol  
817 (Gibco). Half of the medium was replenished on days *in vitro* (DIV) 1 and 3. On DIV 5, half of  
818 the medium was replaced in the morning. In the afternoon, the medium was again replaced  
819 with half serum-free medium containing 75.000 cells from patient-derived low- (“UCSF-UKE-  
820 1”) or high-neural (“UCSF-UKE-2”) cell cultures. Cells were cultured with neurons for 72 h and  
821 then fixed with 4% paraformaldehyde (PFA) for 20 min at room temperature and stained for  
822 puncta quantification as described above.

823

### 824 ***EdU Proliferation Assay***

825 For EdU proliferation assays, coverslips were prepared as described above. Again, at DIV 5,  
826 low-neural (“UCSF-UKE-1”) or high-neural (“UCSF-UKE-2”) glioblastoma cells were added to  
827 the neuron cultures. Forty-eight hours after addition of glioblastoma cells, slides were treated  
828 with 10  $\mu\text{M}$  EdU. Cells were fixed after an additional 24 h using 4% PFA and stained using the  
829 Click-iT EdU kit and protocol (Invitrogen). Proliferation index was then determined by

830 quantifying the percentage of EdU labelled glioblastoma cells (identified by EdU<sup>+</sup>/DAPI<sup>+</sup>) over  
831 total number of glioblastoma cells using confocal microscopy.

832

### 833 **3D Migration Assay**

834 3D migration experiments were performed as previously described (Vinci et al., Methods Mol.  
835 Biol. 2013) with some modifications. Briefly, 96-well flat-bottomed plates (Falcon) were coated  
836 with 2.5µg per 50µl laminin per well (Thermo Fisher) in sterile water. After coating, a total of  
837 200µl of culture medium per well was added to each well. A total of 100µl of medium was  
838 taken from 96-well round bottom ULA plates containing ~200µm diameter neurospheres of  
839 low- (“UCSF-UKE-1”) and high-neural (“UCSF-UKE-2”) glioblastoma lines, and the remaining  
840 medium including neurospheres was transferred into the pre-coated plates. Images were then  
841 acquired using an Evos M5000 microscope (Thermo Fisher Scientific) at time zero, 24, 48,  
842 and 72 hours after encapsulation. Image analysis was performed using ImageJ by measuring  
843 the diameter of the invasive area. The extent of cell migration on the laminin was measured  
844 for six replicate wells normalized to the diameter of each spheroid at time zero and the data is  
845 presented as a mean ratio for three biological replicates.

846

### 847 **Patient Cohorts**

848 In this study, several patients’ cohorts depending on the glioma subclass were analyzed. First,  
849 a clinical cohort of 363 patients who underwent *IDH*-wildtype glioblastoma resection at  
850 University Medical Center Hamburg-Eppendorf, University Hospital Frankfurt, or Charité  
851 University Hospital Berlin (all Germany) was analyzed. Informed written consent was obtained  
852 from all patients and experiments were approved by the medical ethics committee of the  
853 Hamburg chamber of physicians (PV4904). Second, we included patients from the GBM-  
854 TCGA cohort for external validation<sup>18</sup>. Third, a clinical cohort of pediatric and adolescent  
855 patients who underwent surgery for *H3 K27*-altered DMG at University Medical Center  
856 Hamburg-Eppendorf (Germany) was established and extended with two cohorts from

857 previously published studies by Sturm et al. and Chen et al.<sup>29,36</sup>. Last, the reference and  
858 diagnostic set (n=3905) published by Capper et al. was used for deconvolution analyses<sup>17</sup>.

859

## 860 ***Clinical Definitions***

861 For the internal clinical patients cohort, diagnosis was based on the WHO classification.<sup>71</sup> The  
862 extent of resection (EOR) was stratified into gross total resection (GTR), near GTR, and partial  
863 resection (PR). A GTR was defined as a complete removal of contrast-enhancing parts, a near  
864 GTR as a removal of more than 90% of the contrast-enhancing parts, whereas a resection of  
865 lower than 90% was defined as PR/biopsy. The EOR of contrast-enhancing parts was  
866 evaluated by MRI performed up to 48 h after index surgery. Overall survival (OS) was  
867 calculated from diagnosis until death or last follow-up, and progression-free survival (PFS)  
868 from diagnosis until progression according to Response Assessment in Neuro-Oncology  
869 (RANO) criteria based on local assessment<sup>72</sup>. Seizures and use of antiepileptic medication  
870 were defined according to the current guidelines of the International League Against Epilepsy  
871 (ILAE)<sup>73</sup>. For 3D volumetric segmentation, we analyzed T1-weighted as well as T2-weighted  
872 FLAIR (fluid attenuated inversion recovery) magnetic resonance imaging (MRI) axial images  
873 of glioblastoma patients before surgery. The program BRAINLAB was used for all analyses.  
874 To measure tumor volume, the tumor region of interest was delineated with the tool “Smart  
875 Brush” in every slice by hand, enabling a multiplanar 3D reconstruction. With this  
876 methodology, the volume of contrast enhancement, FLAIR hyperintensity, and necrotic  
877 volume was assessed in cm<sup>3</sup>.

878

879

880

881

882

883

## 884 ***Stereotactic Biopsies for Spatial Sample Collection***

885 Biopsies were obtained using a cranial navigation system (Brainlab AG,  
886 Munich, Germany) and intraoperative neuronavigation. To limit the influence of brain shift,  
887 biopsies were obtained before tumor removal at the beginning of surgery with minimal dural  
888 opening. Tissue samples were then transferred to 10% buffered formalin and sent to the  
889 Department of Neuropathology for further processing and histopathological evaluation.

890

## 891 ***Measurement of Functional Connectivity using Magnetoencephalography***

892 Tumor tissues with high (HFC) and low (LFC) functional connectivity sampled during surgery  
893 based on preoperative magnetoencephalography (MEG) were obtained from *IDH*-wildtype  
894 glioblastoma patients operated in the Department of Neurosurgery, University of California,  
895 San Francisco as described previously<sup>10</sup>. From each formalin-fixed paraffin-embedded (FFPE)  
896 tissue block, 4 serial sections of an approximate thickness of 10  $\mu\text{m}$  (in total 40  $\mu\text{m}$ ) were used  
897 for DNA extraction. DNA was extracted with the QIAamp DNA FFPE Kit™ (QIAGEN). DNA  
898 was quantified using the Nanodrop Spectrophotometer (Thermo Scientific). The ratio of OD at  
899 260 nm to OD 280 nm was calculated and served as criteria for DNA quality.

900

## 901 ***Functional Connectivity by Resting-State Functional Magnetic Resonance***

### 902 ***Imaging***

903 44 treatment-naïve glioblastoma patients (mean age: 65 $\pm$ 9 years) underwent resting-state  
904 functional magnetic resonance imaging (rsfMRI) before surgery and tumor tissues were  
905 analyzed for genome-wide DNA methylation patterns using the Illumina EPIC (850k) array.  
906 Functional data were preprocessed using SPM12<sup>74</sup> as implemented in Matlab 9.5 according  
907 to an imaging protocol that was similarly applied and described in previous publications<sup>75,76</sup>.  
908 Briefly, functional images were realigned to the mean functional volume, unwarped and  
909 coregistrated to the structural image. Structural and functional images were segmented, bias  
910 corrected and spatially normalized (multi-spectral classification), and functional images were

911 smoothed with a 5 mm FWHM Gaussian kernel. Functional images were then slice-time  
912 corrected, movement-related time series were regressed out with ICA-AROMA<sup>77</sup>, and data  
913 were high-pass filtered (> 0.01 Hz). Contrast-enhancing tumor lesions were segmented semi-  
914 automatically using the ITK-SNAP software version 3.4.0<sup>78</sup> and used as region of interest  
915 (ROI) to perform a seed-based correlation analysis and compute the voxel-based tumor to  
916 peritumoral connectivity (Fisher z transformation). A 10mm peritumoral distance mask was  
917 created by dilating the tumor mask by 10mm and subtracting the tumor area. The mean  
918 functional connectivity between tumor and its 10mm peritumoral surrounding was computed  
919 using a ROI-to-voxel approach.

920

### 921 ***Drug Sensitivity Analysis***

922 The patient-derived low-neural spheroid glioblastoma cell lines GS-11, GS-73, GS-84 and GS-  
923 110 as well as the high-neural ones GS-13, GS-74, GS-80, GS-90 and GS-101 (Extended  
924 Data 6) were dissociated into single cells and were seeded in Neurobasal medium  
925 supplemented with B27, 1% Glutamine, 1% Pen/Strep, 1uL/mL Heparin and 20 ng/mL human  
926 FGF and EGF at 1250-7500 cells/well into a clear-bottom, tissue-culture treated 384-well plate  
927 (Perkin Elmer, Waltham, Massachusetts, USA). The cells were treated in triplicates with 27  
928 drugs and with DMSO as a control for 48 hours at 37°C and 5% CO<sub>2</sub>. Afterwards the cells  
929 were fixed with 4% PFA (Sigma/Aldrich), blocked with PBS containing 5% FBS, 0.1% TritonX  
930 and DAPI (4 ug/mL, #422801, Biolegend) for one hour at room temperature and were stained  
931 with vimentin (#677809, Biolegend), cleaved Caspase 3 (#9604S, Cell Signaling) and TUBB3  
932 (#657406, Biolegend) antibodies overnight at 4°C. The plate was imaged with an Opera  
933 Phenix automated spinning-disk confocal microscope in three z-stacks at 10x magnification  
934 (Perkin Elmer). The maximal intensity projection of the z-stacks was used for segmentation of  
935 the spheroids based on their DAPI staining using CellProfiler 2.2.0. Downstream image  
936 analysis was performed with MATLAB R2021b. Marker positive cells/spheroids were identified  
937 by a linear threshold on the respective channel. The cell counts as well as the average

938 cell/spheroid areas were averaged per condition and compared between drug treatment and  
939 the control group.

940

### 941 ***Statistical Analysis***

942 Gaussian distribution was confirmed by the Shapiro-Wilk normality test. For parametric data,  
943 unpaired two-tailed Student's t-test or one-way ANOVA with Tukey's post hoc tests to  
944 examine pairwise differences were used as indicated. Survival curves were visualized as  
945 results from the Kaplan-Meier method applying two-tailed log rank analyses for analyzing  
946 statistical significance. Multivariate analysis for OS and PFS displaying hazard ratios (HRs),  
947 and 95% confidence interval (CI) were computed for each group using Cox proportional  
948 hazards regression model. All variables associated with OS or PFS with p-value less than 0.05  
949 in univariate analysis were included in the multivariable model. In general, a p-value less than  
950 0.05 was considered statistically significant for all experiments. Statistical analyses and data  
951 illustrations were performed using GraphPad Prism 10. Alluvial plots were graphed with R  
952 studio.

953

954 **Acknowledgement**

955 We thank Lotte Stegat (Department of Neuropathology, University Medical Center Hamburg-  
956 Eppendorf, Germany) for contributing data to the DMG cohort. The authors acknowledge  
957 Sabine Wutke (University Medical Center Hamburg-Eppendorf, Germany) for graphical  
958 assistance. Initial drafts of figures 1a, 4g, and 4m were made with BioRender.com. Lastly, we  
959 thank all the patients who gave informed consent and without whom this research would not  
960 have been possible.

961

962 **Data Availability Statement**

963 Idat files of the clinical cohort (363 glioblastoma patients) will be made available on Gene  
964 Expression Omnibus (GEO) prior to publication. The methylation data provided by Capper et  
965 al. as illustrated in Supplementary figure 1 are accessible under GSE109381. TCGA-GBM  
966 cohort analyzed for external validation and as shown in Figure 1d is accessible under  
967 <https://portal.gdc.cancer.gov/projects/TCGA-GBM>. All other data are available in the article,  
968 source data, or from the corresponding author upon reasonable request.

969

970 **Funding**

971 This study was supported by numerous grants and research funds. F.L.R. received funding  
972 from the German research foundation (DFG RI2616/3-1) and from Illumina Inc., U.S. was  
973 supported by the Fördergemeinschaft Kinderkrebszentrum Hamburg. Experiments conducted  
974 for investigating functional connectivity were supported by NIH grants K08NS110919 and  
975 P50CA097257; Robert Wood Johnson Foundation grant 74259; the UCSF LoGlio Collective  
976 and Resonance Philanthropies; and U19 CA264339, Tom Paquin Brain Cancer Research  
977 Fund to S.H.J., and the Sullivan Brain Cancer Fund to S.K., R.K. and F.H. are funded by the  
978 EU eRare project Maxomod. S.H. and T.B.H. received funding from SFB 1192 B8 and S.B.  
979 was supported by SFB 1192 C3. M.M. was supported by grants from the National Institute  
980 of Neurological Disorders and Stroke (R01NS092597), NIH Director's Pioneer Award

981 (DP1NS111132), National Cancer Institute (P50CA165962, R01CA258384, U19CA264504).

982 B.W. was supported by the DFG, SFB 824, subproject B12.

983

#### 984 **Authors Contributions**

985 R.D. and F.L.R. designed, conducted, and interpreted all experiments and analyses. R.K. F.H.

986 T.H. S.B and S.H. performed and analyzed deconvolution, copy number variation and

987 proteomic analysis. M.M. and A.S.R. performed immunoassays quantification of BDNF serum

988 levels. F.L.R., C.M., A.S. and K.L. contributed to cell culture, and extracellular vesicle

989 experiments. A.K.W. and U.S. contributed to DMG cohorts. H.B. calculated DNA tumor purity.

990 J.N. conducted mass spectrometry proteomic profiling. K.J. and D.D. contributed to functional

991 connectivity measured by resting state MRI. R.D., T.S., L.D., Y.Z., M.W., F.L.R., K.W., P.N.H.,

992 D.C., J.O., and P.V. contributed glioblastoma cohorts of each institution. B.W. and J.G.

993 performed stereotactic biopsies for spatial sample collection of human glioblastoma patients.

994 M.M. contributed single-cell RNA sequencing data of DMG and provided equipment for *in vivo*

995 analyses. R.D. and M.B.K. conducted *in vivo* experiments for analyzing tumor burden and

996 puncta synapse quantification and C.M. performed xenografting for survival analysis. R.D.

997 performed co-culture experiments and migration assays. L.N. performed electron microscopy

998 images which were evaluated by R.D.. D.S., V.H., and M.L.S. performed cell state composition

999 analysis. S.K. and S.H.J. contributed to functional connectivity measured by MEG. D.H.H.

1000 performed spatial transcriptomics. M.W., B.S., A.B., and T.W. conducted drug sensitivity

1001 analysis. R.D. and F.L.R. wrote the manuscript. All authors contributed to manuscript editing

1002 and approved the final manuscript version.

1003

#### 1004 **Competing Interests**

1005 M.L.S. is equity holder, scientific co-founder and advisory board member of Immunitas

1006 Therapeutics. M.M. holds equity in MapLight Therapeutics.

1007



1008 **REFERENCES**

1009

1010 1. Winkler, F. *et al.* Cancer neuroscience: State of the field, emerging directions. *Cell* **186**,  
1011 1689–1707 (2023).

1012 2. Monje, M. Synaptic Communication in Brain Cancer. *Cancer Res.* **80**, 2979–2982  
1013 (2020).

1014 3. Venkatesh, H. S. *et al.* Electrical and synaptic integration of glioma into neural circuits.  
1015 *Nature* **573**, 539–545 (2019).

1016 4. Venkatesh, H. S. *et al.* Neuronal Activity Promotes Glioma Growth through Neuroligin-3  
1017 Secretion. *Cell* **161**, 803–816 (2015).

1018 5. Venkatesh, H. S. *et al.* Targeting neuronal activity-regulated neuroligin-3 dependency in  
1019 high-grade glioma. *Nature* **549**, 533–537 (2017).

1020 6. Venkataramani, V. *et al.* Glutamatergic synaptic input to glioma cells drives brain tumour  
1021 progression. *Nature* **573**, 532–538 (2019).

1022 7. Campbell, S. L., Buckingham, S. C. & Sontheimer, H. Human glioma cells induce  
1023 hyperexcitability in cortical networks. *Epilepsia* **53**, 1360–1370 (2012).

1024 8. Campbell, S. L. *et al.* GABAergic disinhibition and impaired KCC2 cotransporter activity  
1025 underlie tumor-associated epilepsy. *Glia* **63**, 23–36 (2015).

1026 9. Buckingham, S. C. *et al.* Glutamate release by primary brain tumors induces epileptic  
1027 activity. *Nat. Med.* **17**, 1269–1274 (2011).

1028 10. Krishna, S. *et al.* Glioblastoma remodelling of human neural circuits decreases survival.  
1029 *Nature* **617**, 599–607 (2023).

1030 11. Venkataramani, V. *et al.* Disconnecting multicellular networks in brain tumours. *Nat. Rev.*  
1031 *Cancer* **22**, 481–491 (2022).

1032 12. Shi, D. D. *et al.* Therapeutic avenues for cancer neuroscience: translational frontiers and  
1033 clinical opportunities. *Lancet Oncol.* **23**, e62–e74 (2022).

1034 13. Venkataramani, V. *et al.* Glioblastoma hijacks neuronal mechanisms for brain invasion.  
1035 *Cell* **185**, 2899–2917.e31 (2022).

- 1036 14. Varn, F. S. *et al.* Glioma progression is shaped by genetic evolution and  
1037 microenvironment interactions. *Cell* **185**, 2184-2199.e16 (2022).
- 1038 15. Huang-Hobbs, E. *et al.* Remote neuronal activity drives glioma progression through  
1039 SEMA4F. *Nature* (2023) doi:10.1038/s41586-023-06267-2.
- 1040 16. Moss, J. *et al.* Comprehensive human cell-type methylation atlas reveals origins of  
1041 circulating cell-free DNA in health and disease. *Nat. Commun.* **9**, 5068 (2018).
- 1042 17. Capper, D. *et al.* DNA methylation-based classification of central nervous system  
1043 tumours. *Nature* **555**, 469–474 (2018).
- 1044 18. The Cancer Genome Atlas Research Network. Comprehensive genomic characterization  
1045 defines human glioblastoma genes and core pathways. *Nature* **455**, 1061–1068 (2008).
- 1046 19. Südhof, T. C. Towards an Understanding of Synapse Formation. *Neuron* **100**, 276–293  
1047 (2018).
- 1048 20. Ravi, V. M. *et al.* Spatially resolved multi-omics deciphers bidirectional tumor-host  
1049 interdependence in glioblastoma. *Cancer Cell* **40**, 639-655.e13 (2022).
- 1050 21. Kleshchevnikov, V. *et al.* Cell2location maps fine-grained cell types in spatial  
1051 transcriptomics. *Nat. Biotechnol.* **40**, 661–671 (2022).
- 1052 22. Volker Hovestadt, M. Z. conumee. (2017) doi:10.18129/B9.BIOC.CONUMEE.
- 1053 23. Vaubel, R. A. *et al.* Genomic and Phenotypic Characterization of a Broad Panel of  
1054 Patient-Derived Xenografts Reflects the Diversity of Glioblastoma. *Clin. Cancer Res. Off.*  
1055 *J. Am. Assoc. Cancer Res.* **26**, 1094–1104 (2020).
- 1056 24. Golebiewska, A. *et al.* Patient-derived organoids and orthotopic xenografts of primary  
1057 and recurrent gliomas represent relevant patient avatars for precision oncology. *Acta*  
1058 *Neuropathol. (Berl.)* **140**, 919–949 (2020).
- 1059 25. Romero-Garcia, R. *et al.* Transcriptomic and connectomic correlates of differential  
1060 spatial patterning among gliomas. *Brain J. Neurol.* **146**, 1200–1211 (2023).
- 1061 26. Barthel, F. P. *et al.* Longitudinal molecular trajectories of diffuse glioma in adults. *Nature*  
1062 **576**, 112–120 (2019).

- 1063 27. Stupp, R. *et al.* Radiotherapy plus Concomitant and Adjuvant Temozolomide for  
1064 Glioblastoma. *N. Engl. J. Med.* **352**, 987–996 (2005).
- 1065 28. Drexler, R. *et al.* DNA methylation subclasses predict the benefit from gross total tumor  
1066 resection in IDH-wildtype glioblastoma patients. *Neuro-Oncol.* noac177 (2022)  
1067 doi:10.1093/neuonc/noac177.
- 1068 29. Sturm, D. *et al.* Hotspot Mutations in H3F3A and IDH1 Define Distinct Epigenetic and  
1069 Biological Subgroups of Glioblastoma. *Cancer Cell* **22**, 425–437 (2012).
- 1070 30. Karschnia, P. *et al.* Prognostic validation of a new classification system for extent of  
1071 resection in glioblastoma: A report of the RANO *resect* group. *Neuro-Oncol.* noac193  
1072 (2022) doi:10.1093/neuonc/noac193.
- 1073 31. Ricklefs, F. L. *et al.* Imaging flow cytometry facilitates multiparametric characterization of  
1074 extracellular vesicles in malignant brain tumours. *J. Extracell. Vesicles* **8**, 1588555  
1075 (2019).
- 1076 32. Spelat, R. *et al.* The dual action of glioma-derived exosomes on neuronal activity:  
1077 synchronization and disruption of synchrony. *Cell Death Dis.* **13**, 705 (2022).
- 1078 33. Taylor, K. R. *et al.* *Glioma synapses recruit mechanisms of adaptive plasticity.*  
1079 <http://biorxiv.org/lookup/doi/10.1101/2021.11.04.467325> (2021)  
1080 doi:10.1101/2021.11.04.467325.
- 1081 34. Bumb, J. M. *et al.* Focus on ECT seizure quality: serum BDNF as a peripheral biomarker  
1082 in depressed patients. *Eur. Arch. Psychiatry Clin. Neurosci.* **265**, 227–232 (2015).
- 1083 35. Rocha, R. B. *et al.* Increased BDNF levels after electroconvulsive therapy in patients  
1084 with major depressive disorder: A meta-analysis study. *J. Psychiatr. Res.* **83**, 47–53  
1085 (2016).
- 1086 36. Chen, L. H. *et al.* The integrated genomic and epigenomic landscape of brainstem  
1087 glioma. *Nat. Commun.* **11**, 3077 (2020).
- 1088 37. Mancusi, R. & Monje, M. The neuroscience of cancer. *Nature* **618**, 467–479 (2023).
- 1089 38. Neftel, C. *et al.* An Integrative Model of Cellular States, Plasticity, and Genetics for  
1090 Glioblastoma. *Cell* **178**, 835–849.e21 (2019).

- 1091 39. Singh, O., Pratt, D. & Aldape, K. Immune cell deconvolution of bulk DNA methylation  
1092 data reveals an association with methylation class, key somatic alterations, and cell  
1093 state in glial/glioneuronal tumors. *Acta Neuropathol. Commun.* **9**, 148 (2021).
- 1094 40. Wu, Y. *et al.* Glioblastoma epigenome profiling identifies SOX10 as a master regulator of  
1095 molecular tumour subtype. *Nat. Commun.* **11**, 6434 (2020).
- 1096 41. Shapiro, J. R. & Shapiro, W. R. The subpopulations and isolated cell types of freshly  
1097 resected high grade human gliomas: Their influence on the tumor's evolution in vivo and  
1098 behavior and therapy in vitro. *Cancer Metastasis Rev.* **4**, 107–124 (1985).
- 1099 42. van Kessel, E. *et al.* Tumor-related molecular determinants of neurocognitive deficits in  
1100 patients with diffuse glioma. *Neuro-Oncol.* **24**, 1660–1670 (2022).
- 1101 43. Greenberg, M. E., Xu, B., Lu, B. & Hempstead, B. L. New insights in the biology of BDNF  
1102 synthesis and release: implications in CNS function. *J. Neurosci. Off. J. Soc. Neurosci.*  
1103 **29**, 12764–12767 (2009).
- 1104 44. Tao, X., Finkbeiner, S., Arnold, D. B., Shaywitz, A. J. & Greenberg, M. E. Ca<sup>2+</sup> influx  
1105 regulates BDNF transcription by a CREB family transcription factor-dependent  
1106 mechanism. *Neuron* **20**, 709–726 (1998).
- 1107 45. Wrann, C. D. *et al.* Exercise induces hippocampal BDNF through a PGC-1 $\alpha$ /FNDC5  
1108 pathway. *Cell Metab.* **18**, 649–659 (2013).
- 1109 46. Wang, X. *et al.* Reciprocal Signaling between Glioblastoma Stem Cells and  
1110 Differentiated Tumor Cells Promotes Malignant Progression. *Cell Stem Cell* **22**, 514-  
1111 528.e5 (2018).
- 1112 47. Drexler, R. *et al.* Targeted anticonvulsive treatment of IDH-wildtype glioblastoma based  
1113 on DNA methylation subclasses. *Neuro-Oncol.* noad014 (2023)  
1114 doi:10.1093/neuonc/noad014.
- 1115 48. Ricklefs, F. L. *et al.* DNA methylation subclass receptor tyrosine kinase II (RTK II) is  
1116 predictive for seizure development in glioblastoma patients. *Neuro-Oncol.* noac108  
1117 (2022) doi:10.1093/neuonc/noac108.

- 1118 49. Nejo, T. *et al.* Abstract 2497: Glioma-induced neuronal remodeling promotes regional  
1119 immunosuppression. *Cancer Res.* **83**, 2497–2497 (2023).
- 1120 50. Capper, D. *et al.* Practical implementation of DNA methylation and copy-number-based  
1121 CNS tumor diagnostics: the Heidelberg experience. *Acta Neuropathol. (Berl.)* **136**, 181–  
1122 210 (2018).
- 1123 51. Brat, D. J. *et al.* cIMPACT-NOW update 3: recommended diagnostic criteria for ‘Diffuse  
1124 astrocytic glioma, IDH-wildtype, with molecular features of glioblastoma, WHO grade IV’.  
1125 *Acta Neuropathol. (Berl.)* **136**, 805–810 (2018).
- 1126 52. Bady, P., Delorenzi, M. & Hegi, M. E. Sensitivity Analysis of the MGMT-STP27 Model  
1127 and Impact of Genetic and Epigenetic Context to Predict the MGMT Methylation Status  
1128 in Gliomas and Other Tumors. *J. Mol. Diagn. JMD* **18**, 350–361 (2016).
- 1129 53. Aryee, M. J. *et al.* Minfi: a flexible and comprehensive Bioconductor package for the  
1130 analysis of Infinium DNA methylation microarrays. *Bioinformatics* **30**, 1363–1369 (2014).
- 1131 54. Van Paemel, R. *et al.* Genome-wide study of the effect of blood collection tubes on the  
1132 cell-free DNA methylome. *Epigenetics* **16**, 797–807 (2021).
- 1133 55. Neuberger, E. W. I. *et al.* Physical activity specifically evokes release of cell-free DNA  
1134 from granulocytes thereby affecting liquid biopsy. *Clin. Epigenetics* **14**, 29 (2022).
- 1135 56. Langfelder, P. & Horvath, S. WGCNA: an R package for weighted correlation network  
1136 analysis. *BMC Bioinformatics* **9**, 559 (2008).
- 1137 57. Yip, A. M. & Horvath, S. Gene network interconnectedness and the generalized  
1138 topological overlap measure. *BMC Bioinformatics* **8**, 22 (2007).
- 1139 58. Morabito, S., Reese, F., Rahimzadeh, N., Miyoshi, E. & Swarup, V. hdWGCNA identifies  
1140 co-expression networks in high-dimensional transcriptomics data. *Cell Rep. Methods* **3**,  
1141 100498 (2023).
- 1142 59. Wu, T. *et al.* clusterProfiler 4.0: A universal enrichment tool for interpreting omics data.  
1143 *The Innovation* **2**, 100141 (2021).
- 1144 60. Ruiz-Moreno, C. *et al.* Harmonized single-cell landscape, intercellular crosstalk and  
1145 tumor architecture of glioblastoma.

- 1146 <http://biorxiv.org/lookup/doi/10.1101/2022.08.27.505439> (2022)
- 1147 doi:10.1101/2022.08.27.505439.
- 1148 61. Miller, B. F., Bambah-Mukku, D., Dulac, C., Zhuang, X. & Fan, J. Characterizing spatial  
1149 gene expression heterogeneity in spatially resolved single-cell transcriptomic data with  
1150 nonuniform cellular densities. *Genome Res.* **31**, 1843–1855 (2021).
- 1151 62. Csardi, G., & Nepusz, T. The Igraph Software Package for Complex Network Research.  
1152 InterJournal, Complex Systems, 1695, 1-9. <http://igraph.org>. (2006).
- 1153 63. Pedersen T. ggraph: An Implementation of Grammar of Graphics for Graphs and  
1154 Networks. <https://ggraph.data-imaginist.com>, <https://github.com/thomasp85/ggraph>.  
1155 (2022).
- 1156 64. Silverbush, D., Suva, M. & Hovestadt, V. LTBK-08. Inferring cell type and cell state  
1157 composition in glioblastoma from bulk DNA methylation profiles using multi-omic single-  
1158 cell analyses. *Neuro-Oncol.* **24**, vii300 (2022).
- 1159 65. EpiDISH - Epigenetic Dissection of Intra-Sample-Heterogeneity.  
1160 [https://www.bioconductor.org/packages/devel/bioc/vignettes/EpiDISH/inst/doc/EpiDISH](https://www.bioconductor.org/packages/devel/bioc/vignettes/EpiDISH/inst/doc/EpiDISH.html).  
1161 html.
- 1162 66. Johann, P. D., Jäger, N., Pfister, S. M. & Sill, M. RF\_Purify: a novel tool for  
1163 comprehensive analysis of tumor-purity in methylation array data based on random  
1164 forest regression. *BMC Bioinformatics* **20**, 428 (2019).
- 1165 67. Carter, S. L. *et al.* Absolute quantification of somatic DNA alterations in human cancer.  
1166 *Nat. Biotechnol.* **30**, 413–421 (2012).
- 1167 68. Maire, C. L. *et al.* Genome-wide methylation profiling of glioblastoma cell-derived  
1168 extracellular vesicle DNA allows tumor classification. *Neuro-Oncol.* **23**, 1087–1099  
1169 (2021).
- 1170 69. Hughes, C. S. *et al.* Single-pot, solid-phase-enhanced sample preparation for proteomics  
1171 experiments. *Nat. Protoc.* **14**, 68–85 (2019).
- 1172 70. Kuleshov, M. V. *et al.* Enrichr: a comprehensive gene set enrichment analysis web  
1173 server 2016 update. *Nucleic Acids Res.* **44**, W90–W97 (2016).

- 1174 71. Louis, D. N. *et al.* The 2016 World Health Organization Classification of Tumors of the  
1175 Central Nervous System: a summary. *Acta Neuropathol. (Berl.)* **131**, 803–820 (2016).
- 1176 72. Wen, P. Y. *et al.* Updated Response Assessment Criteria for High-Grade Gliomas:  
1177 Response Assessment in Neuro-Oncology Working Group. *J. Clin. Oncol.* **28**, 1963–  
1178 1972 (2010).
- 1179 73. Scheffer, I. E. *et al.* ILAE classification of the epilepsies: Position paper of the ILAE  
1180 Commission for Classification and Terminology. *Epilepsia* **58**, 512–521 (2017).
- 1181 74. Friston, K. J. *Statistical parametric mapping: the analysis of functional brain images.*  
1182 (Academic Press, 2011).
- 1183 75. Jütten, K. *et al.* Dissociation of structural and functional connectomic coherence in  
1184 glioma patients. *Sci. Rep.* **11**, 16790 (2021).
- 1185 76. Jütten, K. *et al.* Asymmetric TUMOR-RELATED alterations of NETWORK-SPECIFIC intrinsic  
1186 functional connectivity in glioma patients. *Hum. Brain Mapp.* **41**, 4549–4561 (2020).
- 1187 77. Pruim, R. H. R. *et al.* ICA-AROMA: A robust ICA-based strategy for removing motion  
1188 artifacts from fMRI data. *NeuroImage* **112**, 267–277 (2015).
- 1189 78. Yushkevich, P. A. *et al.* User-guided 3D active contour segmentation of anatomical  
1190 structures: Significantly improved efficiency and reliability. *NeuroImage* **31**, 1116–1128  
1191 (2006).
- 1192

## 1193 **FIGURE LEGENDS**

1194

### 1195 **Figure 1:**

#### 1196 **a.) Schematic of study workflow.**

1197 In human subjects (n=5047) diagnosed with a central nervous system tumor we performed  
1198 deconvolution using DNA methylation arrays (850k or 450k) for determining the neural  
1199 signature. *IDH*-wildtype glioblastomas and *H3 K27*-altered diffuse midline gliomas were  
1200 stratified into subgroups with a low- or high-neural signature for further analyses.

1201

#### 1202 **b.) – f.) Survival analysis of glioblastoma patients treated by radiochemotherapy after** 1203 **surgery with a low- and high-neural signature.**

1204 **b.)** Overall survival of 363 glioblastoma patients of the internal clinical cohort.

1205 **c.)** Progression-free survival of 226 glioblastoma patients of the internal clinical cohort.

1206 **d.)** Overall survival of 187 glioblastoma patients of the TCGA-GBM cohort.

1207 **e.) - f.)** Forest plots illustrating multivariate analysis of glioblastoma patients from the  
1208 internal clinical cohort.

1209 *GTR: gross total resection, PR: partial resection, MGMT: O6-methylguanine-DNA-*  
1210 *methyltransferase, OR: odds ratio, CI: confidence interval, TCGA: The Cancer*  
1211 *Genome Atlas.*



1212 **Figure 2: Integrated epigenetic and transcriptomic analysis reveals synaptic**  
1213 **functions and a malignant neural precursor cell-like and oligodendrocyte**  
1214 **precursor cell-like character in high-neural glioblastoma.**

1215

1216 **a.)** Illustration of the workflow to integrate epigenetic and transcriptional data. Gene co-  
1217 regulation networks are correlated to the epigenetic deconvolution signature.

1218 **b.)** Hierarchical dendrogram of the gene expression modules derived from the weighted  
1219 correlation network analysis. On the bottom, Pearson correlation dotplot of the neural  
1220 signature with gene expression models. Size and color indicate the correlation coefficient,  
1221 non-significant correlation is marked.

1222 **c.)** Barplot of the differentially gene expression of module eigengenes (Log2 fold change) in  
1223 low- and high neural glioblastoma (cut-off 0.41).

1224 **d.)** Dimensional reduction (UMAP) of the gene expression modules (named by colors) and **e.)**  
1225 a detailed visualization of the modules: green, cyan and midnightblue (significantly associated  
1226 with high-neural tumors).

1227 **f.)** Gene ontology analysis of gene expression modules in low- and high-neural tumors.

1228 **g.)** UMAP dimensional reduction of the GBMap reference dataset. Colors indicate the different  
1229 cell types.

1230 **h.)** Module eigengene expression of low- and high-neural glioblastoma in the GBMap  
1231 reference dataset.

1232 **i.)** Gene expression enrichment of low- and high-neural associated module eigengenes across  
1233 glioblastoma cell states.

1234

1235

1236 **Figure 3: Spatial transcriptomic and single-cell deconvolution analysis of low-**  
1237 **and high-neural glioblastoma samples.**

1238

1239 **a.) – b.)** Spatial transcriptomic surface plots of samples epigenetically defined as high (upper  
1240 panel) and low (bottom panel) neural tumors. The colors indicate the spatial expression pattern  
1241 of the module eigengenes. Representative H&E stainings are shown in the upper corner.

1242 **c.)** Spatial correlation analysis of low- and high-neural associated module eigengenes with the  
1243 spatial transcriptomic niches.

1244 **d.)** Hierarchical cell architecture of high (left)- and low (right)-neural glioblastoma. Connections  
1245 of the graph represent the spatial proximity of cell types and the size of the dots indicate the  
1246 total cell type abundance and mapped the three upregulated modules to the infiltrative tumor  
1247 zone.

1248 **e.)** Comparison of abundance of cell states analyzed by reference-free deconvolution between  
1249 newly diagnosed, high-neural, and low-neural glioblastomas.

1250 **f.)** Stem cell-like state significantly correlated with an increase of the neural signature in  
1251 glioblastoma samples.

1252 **g.)** An anticorrelation was seen between the abundance of the immune compartment and the  
1253 neural signature.

1254

1255

1256 **Figure 4: Neural classification is conserved in cell culture, correlates with**  
1257 **survival *in vivo* and high-neural glioblastoma shows increased neuron-to-**  
1258 **glioma synapses.**

1259

1260 **a.) – b.)** Comparison of neural signature between patient’s tumor tissue and cell culture in 17  
1261 glioblastomas.

1262

1263 **c.)** Cell composition analysis represents the abundance of cell states between tumor tissue  
1264 and cell culture.

1265

1266 **d.)** Stability of the epigenetic neural signature during long-term cell culturing. Data were  
1267 obtained from a publicly available dataset (n =6, GSE181314) and in-house (n = 1).

1268

1269 **e.) – f.)** Mice survival after xenografting of patient-derived low- and high-neural glioblastoma  
1270 cells in **e.)** our internal cohort, and **f.)** two combined external cohorts.

1271

1272 **g.)** Primary patient-derived low- and high-neural glioblastoma cell suspensions (n = 1 per  
1273 group) were implanted into premotor cortex (M2) of adult NSG mice (n = 5 mice per group).  
1274 Mice were perfused after 8 weeks of tumor growth and brains sectioned in the coronal plane  
1275 for further immunofluorescence analyses.

1276

1277 **h.)** Representative confocal images of tumor burden in low-neural (upper image) and high-  
1278 neural glioblastoma (bottom image) xenografts. *Human nuclear antigen (HNA), red; Ki67,*  
1279 *green. Scale bars: 1.000  $\mu$ m (overview images) and 200  $\mu$ m (magnified images).*

1280

1281 **i.)** Proliferation index (measured by total number of HNA<sup>+</sup> cells co-labelled with Ki67 divided  
1282 by the total number of HNA<sup>+</sup> tumor cells counted across all areas quantified) in low- and high-

1283 neural glioblastoma bearing mice (n = 5 mice per group). **\*\*P < 0.01, two-tailed Student's t-**  
1284 **test.**

1285 **j.)** Representative confocal image of infiltrated whiter matter of high-neural glioblastoma  
1286 xenograft. White box and arrowheads highlight magnified view of synaptic puncta  
1287 colocalization. *Blue, synapsin-1 (presynaptic puncta); white, neurofilament heavy and medium*  
1288 *(axon); red, nestin (glioma cell processes), green, PSD95 (postsynaptic puncta).* Scale bars:  
1289 *500 μm (upper image) and 250 μm (lower image).*

1290 **k.)** Quantification of the co-localization of presynaptic and postsynaptic markers in low- (n =  
1291 22 regions, 5 mice) and high- (n = 21 regions, 5 mice) neural glioblastoma xenografts. **\*\*\*P <**  
1292 **0.001, two-tailed Student's t-test.**

1293

1294 **l.)** Electron microscopy of patient-derived red fluorescent protein (RFP)-labelled low- and high-  
1295 neural glioblastoma cells xenografted into the mouse hippocampus. Quantification of neuron-  
1296 to-glioma synaptic structures as a percentage of all visualized glioma cell processes (left plot)  
1297 and representative electron microscopy image of neuron-to-glioma process in a high-neural  
1298 glioblastoma xenograft (right image). Asterix denotes immuno-gold particle labelling of RFP.  
1299 Postsynaptic density in RFP<sup>+</sup> tumor cell (pseudo-colored green), synaptic cleft, and vesicles  
1300 in presynaptic neuron (pseudo-colored red) identify synapses. **\*\*P < 0.01, two-tailed Student's**  
1301 **t-test. Scale bar: 200 nm.**

1302

1303 **m.)** Primary patient-derived low- and high-neural glioblastoma cells were co-cultured with  
1304 cortical neurons from CD1-mice at P0 and further analyzed for proliferation and neuron-to-  
1305 glioma synapse formation. Additionally, 3D migration assay was performed using  
1306 monocultures of both cell lines.

1307

1308 **n.)** EdU proliferation index (measured by total number of DAPI<sup>+</sup> cells co-labelled with EdU  
1309 divided by the total number of DAPI<sup>+</sup> tumor cells counted across all areas quantified) in low-  
1310 and high-neural glioblastoma as monocultures and co-cultured with neurons. \*\*\* $P < 0.01$ , ns:  
1311  $P > 0.05$ , two-tailed Student's *t*-test,  $n=3$  biological replicates.  
1312  
1313 **o.)** Quantification of the co-localization of PSD95 (postsynaptic) and synapsin-1 (presynaptic)  
1314 in low- and high-neural glioblastoma cells in co-cultures with neurons. \*\*\* $P < 0.01$ , ns:  $P >$   
1315  $0.05$ , two-tailed Student's *t*-test,  $n=3$  biological replicates.  
1316  
1317 **p.)** 3D migration assay analysis with representative images at time 0 h (left) and 72 h (right)  
1318 of low- and high-neural glioblastoma cells as well as comparison of distance of migration 72 h  
1319 after seeding. \* $P < 0.05$ , two-tailed Student's *t*-test,  $n=3$  biological replicates. Scale bars: 1.000  
1320  $\mu\text{m}$ .

1321

1322 **Figure 5: Association of the neural signature with functional connectivity and**  
1323 **spatiotemporal stability in glioblastoma.**

1324

1325 **a.)** Neural signature in glioblastomas categorized into low (LFC) and high functional  
1326 connectivity (HFC) as defined by magnetoencephalography. *\*P < 0.05, two-tailed Student's t-*  
1327 *test.*

1328

1329 **b.)** Overlap between tumor samples classified to the functional connectivity by Krishna et al.  
1330 and the epigenetic-based neural classification of our study.

1331

1332 **c.)** Correlation of neural signature with degree of glioma to peritumoral connectivity as defined  
1333 by resting state functional magnetic resonance imaging.

1334

1335 **d.)** Correlation between functional connectivity as defined by resting state functional magnetic  
1336 resonance imaging and low- and high-neural glioblastoma groups. *\*P < 0.05, two-tailed*  
1337 *Student's t-test.*

1338

1339 **e.)** Two representative examples of patients with glioblastoma showing the ROI-to-voxel  
1340 functional connectivity of the CE-enhancing area (ROI) to its 10mm peritumoral surrounding.  
1341 Left image shows the peritumoral connectivity of patient with high-neural score (0.457) and  
1342 mean functional connectivity to its peritumoral area of 0.837. In contrast, the right panel shows  
1343 a patient with a low-neural score (0.347) and mean functional connectivity to its peritumoral  
1344 area of 0.294.

1345

1346 **f.) – h.)** Association of neural glioblastoma group with volume of **f.)** contrast-enhancement, **g.)**  
1347 FLAIR, and **h.)** tumor necrosis measured by preoperative magnetic resonance imaging. *\*P <*  
1348 *0.05, ns: P > 0.05, two-tailed Student's t-test.*

1349

1350 i.) Analysis of intertumoral difference of neural signature within 34 newly diagnosed  
1351 glioblastomas with spatial collection of 3 to 7 samples per tumor. 23 (67.6 %) of these tumors  
1352 had a pure low- or high-neural signature in all individual biopsies with additional 10 (29.4 %)  
1353 tumors being predominantly low or high.

1354

1355 j.) Neural signature in 39 patients with matched tumor tissue obtained from surgery at first  
1356 diagnosis and recurrence. *ns:  $P > 0.05$ , two-tailed Student's t-test.*

1357

1358 k.) Sankey plot illustrating a potential switch of the neural subgroup between first diagnosis  
1359 and recurrence.

1360

1361 **Figure 6: Neural classification predicts benefit of extent of resection and *MGMT***  
1362 **promoter methylation status and can be detected in serum of glioblastoma**  
1363 **patients.**

1364

1365 a.) Neural signature in DNA methylation subclasses of newly diagnosed IDH-wildtype  
1366 glioblastoma.

1367

1368 b.) – c.) Survival outcome categorized after extent of resection in glioblastoma patients treated  
1369 by radiochemotherapy with a b.) low- and c.) high-neural tumor.

1370

1371 d.) Survival outcome categorized by *MGMT* promoter methylation status in glioblastoma  
1372 patients treated by radiochemotherapy with a low- and high-neural tumor.

1373

1374 e.) Correlation of neural signature and number of extracellular vesicles in patient serum at  
1375 time of diagnosis.

1376

1377 f.) Comparison of neural signature in healthy individuals, glioblastoma patients, and  
1378 meningioma patients between matched tumor tissue, extracellular vesicle-associated DNA in  
1379 serum, and cell-free DNA in serum.

1380

1381 g.) – h.) Immunoassay quantification of serum BDNF concentration of 94 glioblastoma patients  
1382 and healthy donors as well as meningioma patients as control groups at time of diagnosis. **\*\**P***  
1383 **< 0.01, \*\*\**P* < 0.001, two-tailed Student's *t*-test.**

1384

1385 i.) Cell composition analysis in glioblastoma with low and high BDNF serum levels.

1386



1387 j.) – k.) Seizure outcome of glioblastoma patients considering BDNF serum levels j.) at time  
1388 of surgery, and k.) during follow-up. \* $P < 0.05$ , \*\*\* $P < 0.001$ , two-tailed Student's *t*-test.

1389 **Supplementary figure 1:**

1390 Neural signature in different central nervous system tumor entities (left) and healthy brain

1391 tissues (right) obtained from the Capper dataset<sup>37</sup>.

1392 **Supplementary figure 2:**

1393 Neural signature of all glioblastoma samples. Red line indicates median neural score of all  
1394 1058 included glioblastoma patients and defines the cut-off for stratification into low- and high-  
1395 neural glioblastoma.

1396 **Supplementary figure 3:**

1397 Survival analysis of glioblastoma patients applying brain tumor-related cell signatures

1398 of the Moss signature.

1399 OS: *overall survival*

1400 **Supplementary figure 4: High-neural glioblastoma is linked with synapse**  
1401 **formation and trans-synaptic signaling from methylation and proteomic**  
1402 **profiling.**

1403

1404 a.) Volcano plot showing differentially methylated CpG sites of genes of the invasivity  
1405 signature, neuronal signature, and trans-synaptic signaling signature in high-neural  
1406 glioblastoma.

1407

1408 b.) Correlation between neural signature and DNA tumor purity in glioblastoma samples from  
1409 the clinical cohort.

1410

1411 **c.) – i.) Proteomic profiling of low- and high-neural glioblastoma.**

1412 c.) WGCNA analysis showed differentially abundant proteome modules between both  
1413 neural subgroups.

1414 d.) High-neural glioblastomas are clustered to module “blue” (top figure), while low-  
1415 neural glioblastomas have a higher abundance in module “brown” (bottom figure)

1416 e.) – f.) Network analysis revealed e.) most expressed proteins and f.) associated gene  
1417 ontology terms for each neural subgroup (high-neural: top, low-neural: bottom).

1418 g.) Integrating transcriptomic single-cell data showed an OPC-/NPC-like character in  
1419 high-neural tumors (“ME blue”).

1420 h.) Transcriptomic single-cell CNV plot analysis of glioblastomas with a high-neural signature.

1421 **Supplementary figure 5:**

1422 Copy number variation plots for **a.)** all glioblastoma samples and **b.) – c.)** neural subgroups of

1423 the clinical cohort (n=363).

1424 **Supplementary figure 6:**

1425 **Drug sensitivity analysis of low- and high-neural glioblastoma cells.**

1426 a.) Representative microscopic images for high- (left image) and low-neural (right image)

1427 glioblastoma cells. *Green: Vimentin, yellow: cleaved caspase 3, TUBB3: red, DAPI: blue.*

1428 *Scale bars: 10 $\mu$ m.*

1429 b.) Drug sensitivity of low- and high-neural glioblastoma cells measured by cleaved caspase

1430 3.

1431 c.) Drug sensitivity of low- and high-neural glioblastoma cells measured by average cell area.

1432 d.) Statistical difference of sensitivity to various drugs between low- and high-neural

1433 glioblastoma cells.

1434 **Supplementary figure 7:**

1435 Survival outcome categorized after RANO categories for extent of resection in glioblastoma  
1436 patients treated by radiochemotherapy with a low- and high-neural signature. *Class 1: 0 cm<sup>3</sup>*  
1437 *CE + ≤5 cm<sup>3</sup> nCE tumor, Class 2: ≤1 cm<sup>3</sup> CE, Class 3A: ≤5 cm<sup>3</sup> CE, Class 3B: ≥5 cm<sup>3</sup> CE.*<sup>19</sup>



1438 **Supplementary figure 8: Relevance of neural classification in pediatric and**  
1439 **adolescent patients diagnosed with *H3 K27*-altered diffuse midline glioma**  
1440 **(DMG).**

1441

1442 **a.)** Association of tumor location with neural signature.

1443

1444 **b.)** Volcano plot showing differentially methylated CpG-sites of genes of the invasivity  
1445 signature, neuronal signature, and trans-synaptic signaling signature.

1446

1447 **c.)** Cell state composition analysis in low- and high-neural DMG.

1448

1449 **d.)** Synaptic gene expression (*PTPRS*, *ARHGEF2*, *GRIK2*, *DNM3*, *LRRTM2*, *GRIK5*,  
1450 *NLGN4X*, *NRCAM*, *MAP2*, *INA*, *TMPRSS9*)<sup>6</sup> is significantly correlated with the stem cell-like  
1451 state of DMG cells calculated by an overlap of single cell DNA methylation and single cell RNA  
1452 sequencing (599 cells from 3 study participants) measurements.

1453

1454 **e) – h.)** Kaplan-Meier survival analysis of 72 DMG patients under 18 years of age with a low-  
1455 and high-neural DMG.

1456

1457

1458 **TABLE LEGENDS**

1459

1460 **Supplementary table 1:**

1461 Clinical characteristics of patients with glioblastoma who were treated with combined radio  
1462 chemotherapy after surgical resection.

1463 *SD: standard deviation, MGMT: O6-methylguanine-DNA-methyltransferase*

1464

1465 **Supplementary table 2:**

1466 Uni- and multivariate analysis of overall survival in patients with glioblastoma.

1467 *HR: hazard ratio, CI: confidence interval, Ref: reference, KPS: Karnofsky Performance Scale,*

1468 *GTR: gross total resection, MGMT: O6-methylguanine-DNA-methyltransferase, CE: contrast-*

1469 *enhancement, FLAIR: fluid attenuated inversion recovery, RTK: receptor tyrosine kinase,*

1470 *MES: mesenchymal.*

1471

1472

1473 **Supplementary table 3:**

1474 Uni- and multivariate analysis of progression-free survival in patients with glioblastoma.

1475 *HR: hazard ratio, CI: confidence interval, Ref: reference, KPS: Karnofsky Performance Scale,*

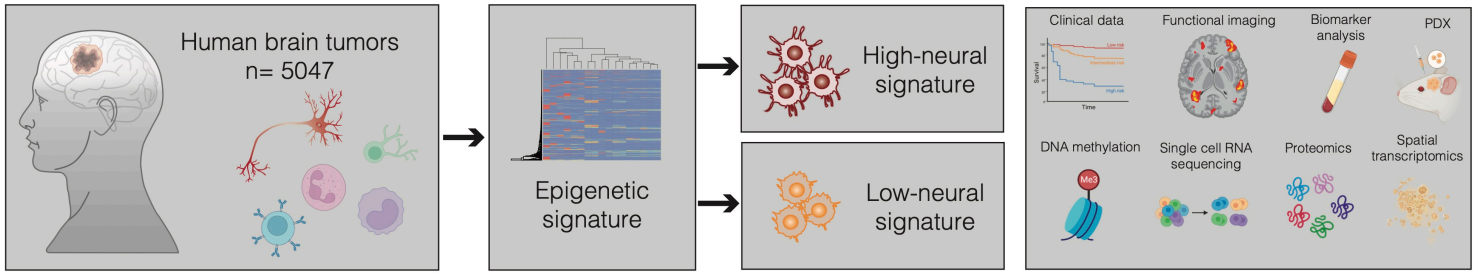
1476 *GTR: gross total resection, MGMT: O6-methylguanine-DNA-methyltransferase, CE: contrast-*

1477 *enhancement, FLAIR: fluid attenuated inversion recovery, RTK: receptor tyrosine kinase,*

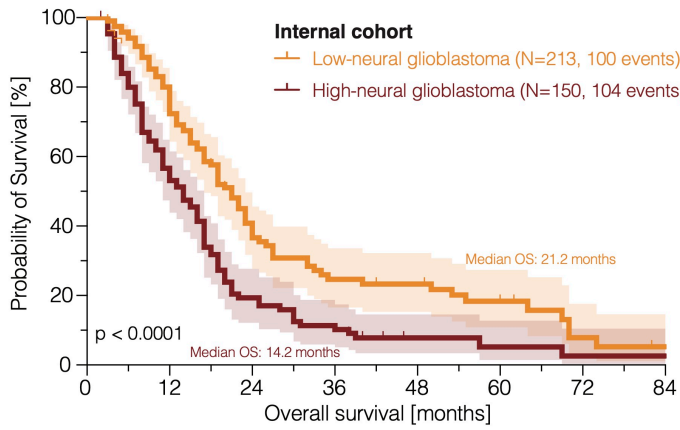
1478 *MES: mesenchymal.*

1479

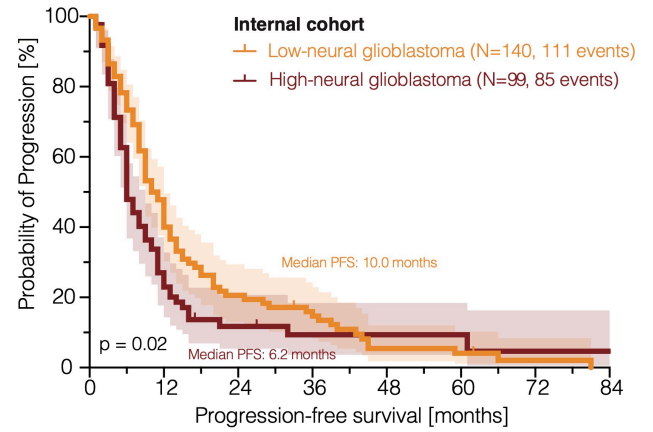
**a**



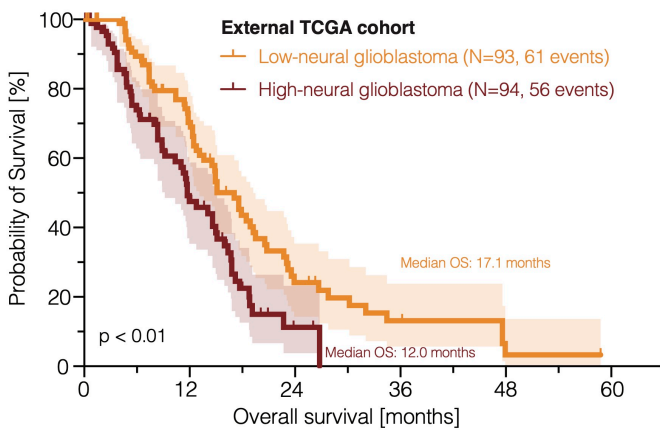
**b**



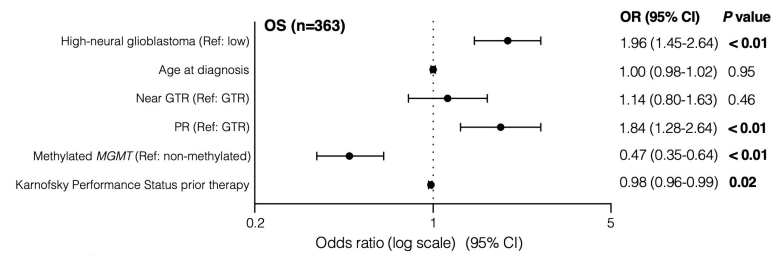
**c**



**d**



**e**



**f**

